Power quality enhancement of microgrid using fuzzy logic controlled inverter and SFCL

Saumen Dhara[1] · Alok Kumar Shrivastav[2] · Pradip Kumar Sadhu[3]

Abstract
This research paper presents a new approach to address power quality concerns in microgrids (MGs) by employing a superconducting fault current limiter (SFCL) and a fuzzy-based inverter. The integration of multiple power electronics converters in a microgrid typically increases total harmonic distortion (THD), which in turn results in power quality issues. Moreover, the intrinsic variability of solar and wind power sources gives rise to fluctuations in power generation, which consequently leads to power oscillations and voltage sag within microgrids that rely on renewable energy. This research paper introduces a technical approach to achieve power balance in renewable-based microgrids (MGs) by utilizing a fuzzy logic-controlled (FLC) pulse width modulation (PWM) inverter. The Microgrid (MG) consists of a hybrid photovoltaic (PV) system and a wind energy conversion system (WECS) that utilizes a permanent magnet synchronous generator (PMSG). The system employs an optimal torque-controlled maximum power point technique (MPPT) algorithm to optimize power output. The battery energy storage system (BESS) is employed to facilitate power provision during critical scenarios or to ensure a stable power output for fluctuating loads. The SFCL is utilized as a device for voltage compensation in cases of voltage sag incidents. The effectiveness of the suggested control strategy is assessed by performing a comparative analysis of total harmonic distortion (THD) in the load voltage, with and without the utilization of a SFCL. The results suggest that the incorporation of an FLC inverter-SFCL-BESS system effectively mitigates THD and voltage sag, according to the requirements set by the IEEE 519 standards. The research study is carried out by using the MATLAB/ SIMULINK software environment.

Abbreviations

SFCL	Superconducting fault current limiter
MGs	Microgrids
THD	Total harmonic distortion
FLC	Fuzzy logic-controlled
PWM	Pulse width modulation
PV	Photovoltaic
PV-WECS	Photovoltaic-wind energy conversion systems
PMSG	Permanent magnet synchronous generator
WECS	Wind energy conversion system
MPPT	Maximum power point technique
BESS	Battery energy storage system
RESs	Renewable energy sources
BS	Battery storage
SVPWM	Space vector pulse width modulation
OT	Optimum torque
PCC	Point of common coupling
WES	Wind energy system
DFIG	Doubly fed induction generator
E	Errors
COE	Change of error
LP	Large positive
MP	Medium positive
SP	Small positive
NE	Negligible error
SN	Small negative
LN	Large negative

✉ Saumen Dhara
  saumen.dhara@gmail.com

  Alok Kumar Shrivastav
  alok5497@gmail.com

  Pradip Kumar Sadhu
  pradip_sadhu@yahoo.co.in

[1] Electrical Engineering Department, Greater Kolkata College of Engineering and Management, Baruipur, Kolkata, West Bengal 743387, India

[2] Electrical Engineering Department, JIS College of Engineering, Kalyani, Nadia 741235, India

[3] Electrical Engineering Department, IIT(ISM), Dhanbad, Jharkhand 826004, India

MN	Medium negative
PFM	Power frequency management
SOC	State of charge
DOD	Depth of discharge
PF	Power factor
VSI	Voltage source inverter
L–G	Single line-to-ground fault
L–L–G	Double line-to-ground fault
L–L–L–G	Triple line-to-ground fault
PFC	Power factor correction
WG	Wind generator

1 Introduction

The global rate of increase in primary energy consumption decelerated to 1.3% in the previous year, representing only half of the growth rate observed in 2018, which stood at 2.8%. The rise in energy consumption is primarily attributed to the utilization of renewable energy sources (RESs), leading to a 0.5% expansion in carbon emissions. This growth rate is less than half of the average annual growth rate of 1.1% observed over the past decade, as reported by the BP statistical review of world energy and others in 2020 (BP statistical review of world energy 2020). This provides a definitive indication that the energy roadmap has shifted its focus towards the utilization of renewable energy sources. In order to meet the growing energy demand with a high level of reliability, it is necessary to further develop and advance renewable energy technologies.

Solar photovoltaic and wind power generation are widely adopted as renewable energy sources for electricity production due to their abundance, cost-effectiveness, and numerous environmental benefits (Xu et al. 2019) (Xiaofeng et al. 2019). The user's text is already technical and does not require any rewriting. The possibility of combining multiple renewable sources with an energy storage system has become feasible due to advancements in power electronics technology. This has led to the development of the microgrid model, as discussed in studies by (Zhao et al. 2010); (Praiselin et al. 2017); (Iqbal and Xin 2020). The predominant renewable energy sources in MG, as documented by (Dhara et al. 2023), are PV and wind power. Nevertheless, due to the inherent intermittency of renewable energy sources, it is recommended to augment them with suitable storage systems and seamlessly integrate them into the microgrid network. In order to optimize the utilization of battery storage (BS) systems in MGs,

numerous investigations were conducted to improve the effectiveness of energy generation and storage devices within the MG. Consequently, a plethora of sophisticated optimization algorithms have been devised. Multi-target integral linear programming is a mathematical optimization technique employed to address a complex problem related to the integration of multiple energy sources, including a hybrid energy supply and a battery source. This approach was proposed by (Zhao et al. 2010). Fuzzy logic control regulates the charging and discharging operations of the battery. Capital and maintenance expenditures, fuel prices, energy expenditures, and carbon penalties are some of the objective functions that need to be minimized.

Renewable energy sources exhibit promising prospects. However, their reliance on weather conditions, such as solar irradiation and wind speed, introduces intermittency. This poses significant challenges for chemical and manufacturing industries, as they are highly susceptible to power fluctuations (Jowder et al. 2009) (F.A.L. Jowder 2009); (Kim et al. 2013) (Kim et al. 2013); (Ullah et al. 2020) (Jan et al. 2020). The majority of power quality issues, accounting for 80% of cases, are caused by harmonics, flickers, and voltage sag and swell. The inclusion of a voltage source inverter within the microgrid results in the production of harmonics (Dhara et al. 2022), which subsequently degrades the power quality of the system. The initiation of high-capacity motors, the act of switching loads, the activation of transformers, and the sporadic behaviour of RESs are the primary factors contributing to voltage sag occurrences (Lii et al. 2004). The SFCL is a highly efficient solution for mitigating issues related to voltage sag, swell, flickers, and harmonic distortion. Previous studies have investigated sag mitigation techniques without the use of energy storage components (Lii et al. 2004); (Ibrahim et al. Sept. 2011); (Kanjiya et al. 2013); (Li et al. Feb. 2018). Additionally, research has been conducted on sag mitigation methods that involve the utilization of battery and super magnetic storage systems (Gee et al., 2017) (Gee et al. March 2017); (Zheng et al. 2018). The BESS is considered a highly effective solution for mitigating disturbances caused by fluctuations in load or generation. This has been supported by studies conducted by (Gil-Antonio et al. 1843); (Dam et al. 2020) (Hannan et al. 2019). The SFCL is utilized for the purpose of enhancing power quality in hybrid photovoltaic-wind energy conversion systems (PV-WECS) as described by Mosaad et al. (2019a); (Muhammad et al. 2020) (Aurangzeb et al. 2020). The authors of (Mosaad et al. 2019b) introduced the SFCL with space vector pulse width modulation (SVPWM) as a solution to address the issues of harmonic distortion and voltage sag reduction. If the SFCL is powered by the primary supply source, it may exhibit suboptimal performance when subjected to significant

voltage sags. The SFCL's performance can be enhanced through the integration of battery energy storage system. PV inverted power is a research paper authored by (Hannan et al. 2019), which discusses various technical aspects related to photovoltaic (PV) systems. These aspects include PV output characteristics, voltage control mechanisms, harmonic mitigation techniques, and overall system performance. Multiple methodologies were explored to mitigate the impact of photovoltaic (PV) deficit, such as the implementation of advanced inverter control systems as discussed by (Gee et al. March 2017). In the realm of advanced research and product development, the paramount requirements for an inverter's control system are high quality and exceptional flexibility. Nevertheless, the commercially available inverters do not produce clean waveforms. Based on the author's understanding, the implementation of the new control strategy remains necessary in order to mitigate harmonic distortion and effectively compensate for voltage flickers, sag, and swell within a hybrid microgrid. This study employs a voltage source inverter (VSI) and a SFCL that are based on fuzzy logic control to address power quality concerns. The voltage source inverter-based FLC demonstrates the ability to mitigate harmonics (Dhara et al. 2022) and prevent their ingress into the load/grid interface. The SFCL system mitigates power fluctuations caused by the unstable output of renewable energy sources and during fault conditions.

A performance analysis is conducted to evaluate the system's behaviour under different load and fault conditions. A comparative analysis of THD is presented, considering the presence and absence of SFCL, specifically focusing on load voltage. Furthermore, the obtained results have undergone a thorough comparison and validation process in accordance with the guidelines set forth by the Institute of Electrical and Electronics Engineers (IEEE) 519 standards. The details pertaining to a prospective microgrid are elaborated upon in Sect. 2. The topic of system modelling is elaborated upon in Sect. 3. Section 4 of the document encompasses the calculation of battery energy loss and provides instructions for power frequency management. The subsequent simulation results and discussions are presented in Sect. 5, while Sect. 4 provides a concise conclusion of the study.

2 Description of hybrid system

The proposed microgrid comprises a hybrid photovoltaic (PV) and wind system that is integrated with a battery storage system. This integrated setup is designed to provide power to an off-grid community. Figure 1 depicts the schematic representation of the proposed microgrid system. The system consists of a photovoltaic (PV) system

connected to a boost converter as well as a permanent magnet synchronous generator with a wind energy conversion system connected to a boost converter. The PMSG-WECS utilizes an optimum torque (OT) based MPPT technique, as described by (Wang et al. 2018). The system consists of a bi-directional (DC-DC) converter that is connected to the BS system. The converter is controlled by a fuzzy-based controller. These three converters are connected to the shared direct current (DC) link with a voltage of 640 V. The fuzzy logic-based voltage source converter (VSC)-controlled inverter is employed for supplying power to the alternating current (AC) loads. Two transformers are employed, with one serving as a step-up transformer to increase the voltage to 11 kV. This elevated voltage is then utilized to provide power to industrial consumers, such as those found in the manufacturing sector. The second transformer is a step-down transformer that provides AC power to the consumer at a voltage of 11/0.380 kV and a frequency of 50 Hz. The SFCL is installed at the point of common coupling (PCC) in order to mitigate unbalanced conditions, voltage fluctuations (sags and swells), and enhance the overall power quality of the system. The discrepancy between the supply side feeder F_1 and the load side feeder F_2 is rectified through the implementation of appropriate voltage injection by a voltage source inverter using an injecting transformer. The transformer operates to maintain the pulsating DC to fixed DC in the circuit. The LC filter circuit is employed to attenuate the undesirable harmonic components. The specifications pertaining to the PV-Wind hybrid microgrid can be found in Table 1 and the proposed microgrid system Simulink diagram is represented in Fig. 2 by selecting all values as per IEEE standard data table.

3 Modelling of the system

3.1 Modelling of the PV system

Figure 3 depicts the PV cell's comparable circuit. The PV cell modeling (Mosaad et al., 2019b) (Mosaad et al 2019b) can be described by the following equations:

$$I = I_L - I_D \left\{ e^{\frac{q(v+IR_s)}{nkT}} - 1 \right\}, \tag{1}$$

and PV power at time t is calculated by Prakash et al. (2014).

$$P_{pv}(t) = S_r(t) * a * \eta. \tag{2}$$

The total PV system power was calculated by (Rehman et al. 2021).
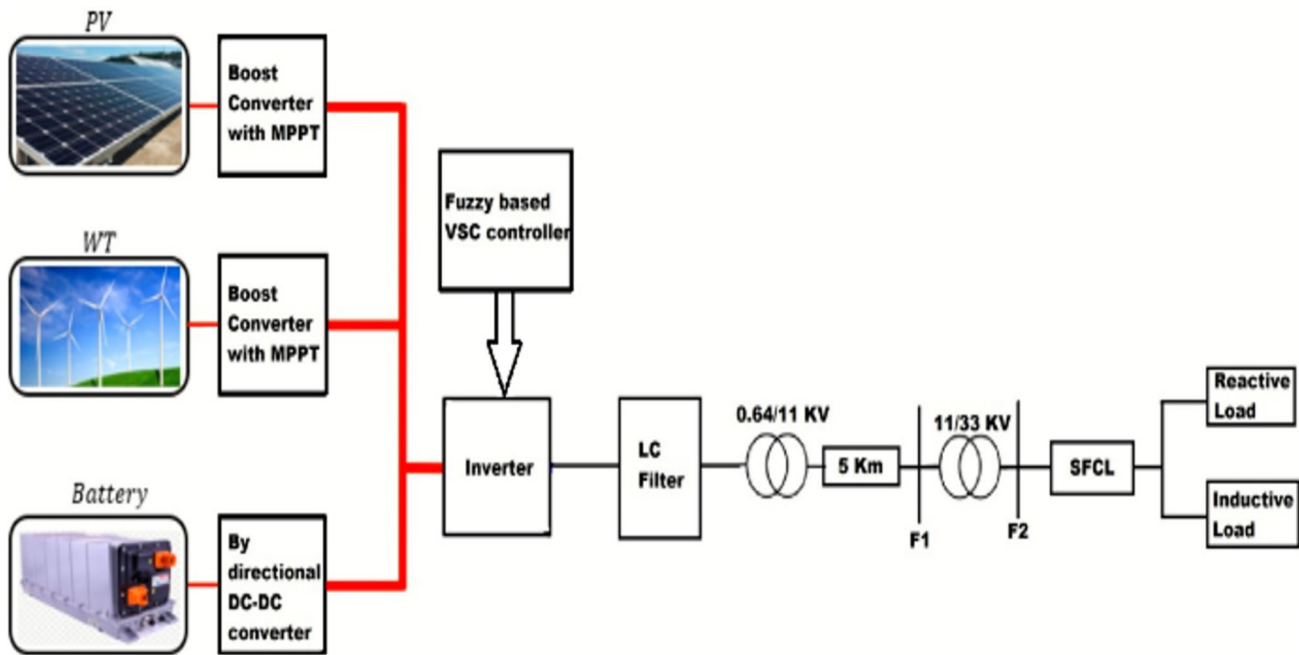
$$P_t(t) = N_{pv} * P_{pv}(t). \tag{3}$$

Fig. 1 The proposed microgrid block diagram

Table 1 Specifications of the PV-Wind hybrid microgrid

Grid subsystem	Ratings
PV system	P_{OUTPUT}= 10,000 W
	V_{MPPT}= 54.7 V
	V_{OC}= 64.2 V
	I_{SC} = 5.96 A
	R_{SERIES}= 0.37125 Ω
	Number of series connected module per string = 11
	Parallel string = 3
Wind energy system (WES)	P_{OUTPUT} = 8.5 kW (For PMSG based WECS, Salient pole)
	Friction factor = 1.111189 Nm/s
	Inertia = 0.01197 kg/m^2
	Viscous damping = 0.001189
Battery system	Ni-Metal-Hydride type
	Rated capacity (Ah) = 6.5
	Nominal voltage (V)= 300
	Initial state of charge = 60%
L-C Filters	Capacitance = 85 μF
	Inductance = 25 mH
SFCL DC voltage &	V_{dc} = 400 V
Injecting transformer ratings	0.48 kV/0.48 kV
	50 Hz

The PV model includes the following parameters:

I_L= Light generated current (A).

I_D = Reverse saturation current of diode (A).

v = Operating voltage of array (V).

k = Boltzmann constant (J/°K).

n = No. of the series connected cell.

T = Temperature (°K).

R_s= Equivalent series resistance (Ω).

R_{sh}= Equivalent shunt resistance (Ω).

q = Charge on electrons.
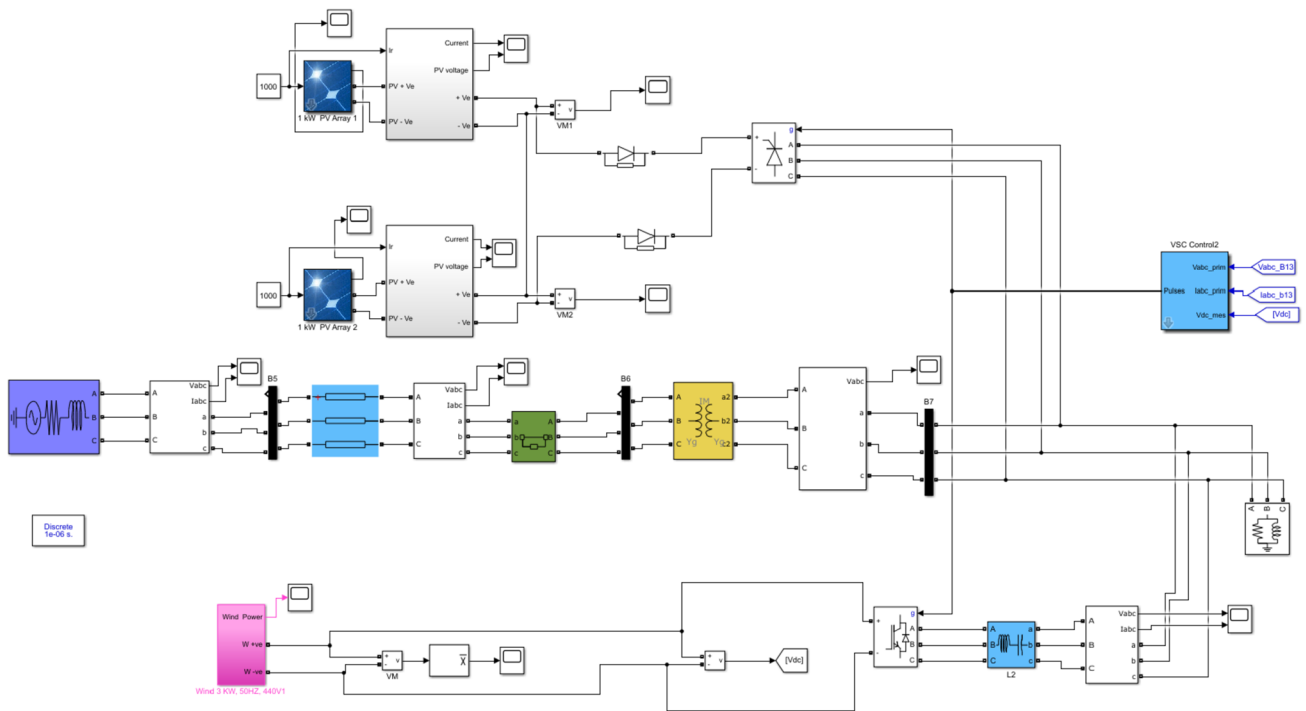
a = Ideality factor.

η = System efficiency.
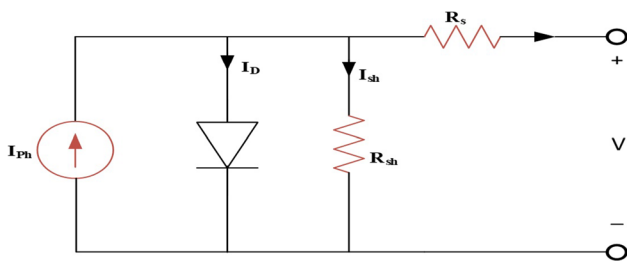
Fig. 2 The proposed microgrid system Simulink diagram

Fig. 3 The PV cell's equivalent circuit

S_r = Solar irradiation during time (t).
N_{pv} = Total no. of the solar module.
P_{pv} = Total power of the solar module.

3.2 Wind turbine modelling

The wind energy system harnesses the mechanical energy derived from the kinetic energy of the wind, which is then employed to power the generator. Various generator configurations are employed in wind energy conversion system. The utilization of the doubly fed induction generator (DFIG) for the purpose of managing active and reactive power through the implementation of direct power control method is demonstrated in the works of (Jou et al. 2009); (Lan et al. 2018). The self-excited induction (Mosaad and Salem 2014) and the doubly excited induction generator

(Mosaad et al. 2019); (Mosaad et al. 2020) have been utilized in various applications of WECS. The permanent magnet synchronous generator demonstrates satisfactory performance under varying wind speeds and operates without the need for gears. This characteristic of the PMSG makes it well-suited for numerous applications.

The PMSG based WECS implemented for off grid hybrid system in Osama abed et al. (2018). In the proposed WECS system, optimal torque (k_{opt}) based MPPT technique is used, to optimize the wind energy efficiency by keeping machine wind generation (ω_g) at predefined optimal value. The model diagram of k_{opt} based controller is presented in Fig. 4. This controller is having the ability to adjust the PMSG torque at optimal torque value at given speed.

To ensure a particular voltage input data or set point, the controller utilizes appropriate control techniques. The harmonic content of the output voltage can be reduced by designing a good control strategy Rehman et al. (2021). The duty cycle of power devices is one of the control factors in power converters. The inverter response voltage can track the reference input voltage signal for controlling the activity cycle Gil-Antonio et al. (1843). The following accuracy is generally determined by the capacity of the control network.

Fig. 4 Block diagram of optimal torque based MPPT controller
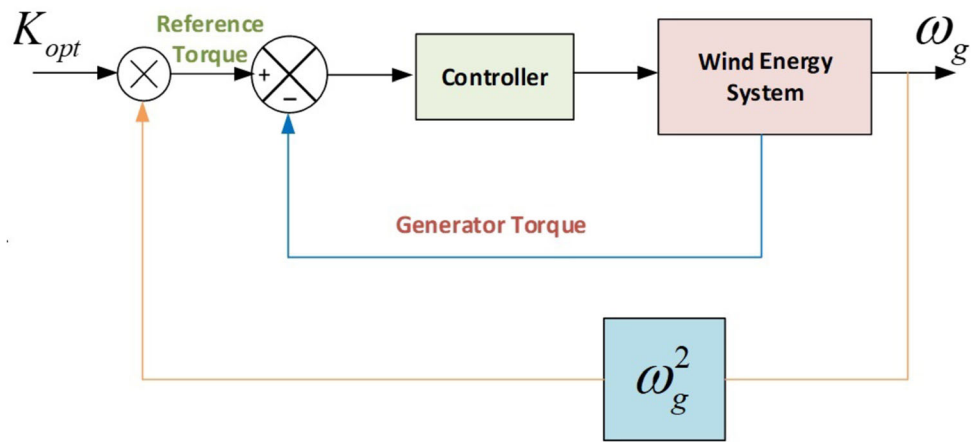
3.3 Illustration of a solar module using a boost chopper

The PV sections that produce the photovoltaic module are linked in a specific order. Each PV section is originated by several PV modules are connected sequentially (Mohomad et al. 2017) (Mohomad et al. 2017). The photovoltaic cell, which is made up of the power supply I_{ph}, a diode D_j, a parallel resistance R_p, and a string resistance R_s, makes up the circuit of the standalone diode depicted in Fig. 5. The resultant current (in Ampere) of the examined photovoltaic range is represented in Eq. (24) by raising the unit of a PV cell to characterize a PV range as illustrated inside (Mosaad et al. (2019a), (Mosaad et al. (2019b). Therefore,

$$I_{pv} = N_{gf}I_p - N_{gf}I_0\left\{exp\left[\frac{q(V_{pv}+R_{qw}I_{pv})}{kATN_pN_{js}}\right]-1\right\} \\ -(V_{pv}+R_{qw}I_{pv})/R_{qa.} \tag{4}$$

Here V_{pv} is the voltage range of photovoltaic module; the corresponding figures of PV units that are normally connected in lines and in parallel, separately, are N_{js} and N_{gf}, the number of successively connected cells in a photovoltaic module is N_p; the parallel resistances are R_{qw} and R_{qa}, correspondingly; and I_{ph} and I_0 are the particular phase current and no-load currents (in A), correspondingly. The representation of specific currents I_{ph} and I_0 are as follows (Mosaad et al. (2019a), Mosaad et al. (2019b):
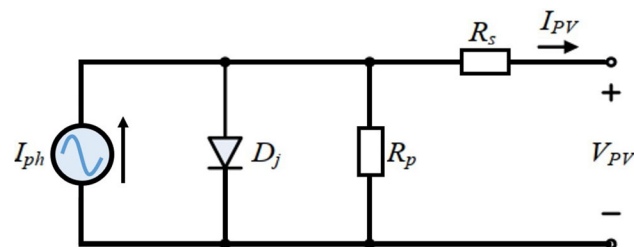
Fig. 5 PV cell circuit for stand-alone use

$$I_{ph} = \left[I_{T,n}+k_i(T_p-T_{pn})\right]\left(\frac{G}{G_n}\right), \tag{5}$$

$$I_0 = I_{T,n}(\frac{T_p}{T_{pn}})^3. \tag{6}$$

In which.

$$I_{0,k} = \frac{I_{sc,k}}{\left\{exp\left[\frac{qV_{oc,k}}{kAT_kN_j}\right]-1\right\}}. \tag{7}$$

In the usual investigated condition of $G_n = 2000W/m^2$ and $T_n = 308.14K(35\ ^0C)$, where T and G stands for photovoltaic radiation (in W/m^2) and operating reversion (in K), respectively; I_{sc} and $V_{oc,k}$ will be the short circuit current (A) and open circuit voltage (V); the reverse saturation power at T_n is denoted by $I_{O,k}$. For illustration, q, k, and also A would be the electron charge (within C), the Boltzmann constant (within J/K), and along with the diode ideality element. The specific space energy associated with the semiconductor would be within e_V. When connecting the photovoltaic range to the DC connection, the specific simplified plan via the analyzed DC-DC boost converter is shown in Fig. 5(a). By pretending that the switch S and diode D exhibit the precise transforming behaviour as shown in Fig. 6(a). The specific upgraded DC-DC converter can be seen in Fig. 6(b). Therefore, the following dynamic computation may be obtained to simulate the specific DC-DC improved converter (Jan et al. 2021); Rehman et al. (2021):

$$(F_c)P_w(V_{pv}) = i_{pv} - i_{LP,} \tag{8}$$

$$(F_L)P_w(i_{LP}) = -R_Pi_{LP} + V_{pv} - (1-K_P)V_{DC} \tag{9}$$

$$i_{pv\_DC} = (1-K_p)i_{LP} \tag{10}$$

where F_c is typically the filter capacitor; i_{pv_DC} is the current of DC-link; L_P and R_P are the particular certain inductance and resistance of the converter, correspondingly; the DC-link voltage is V_{DC}; the inductor current is
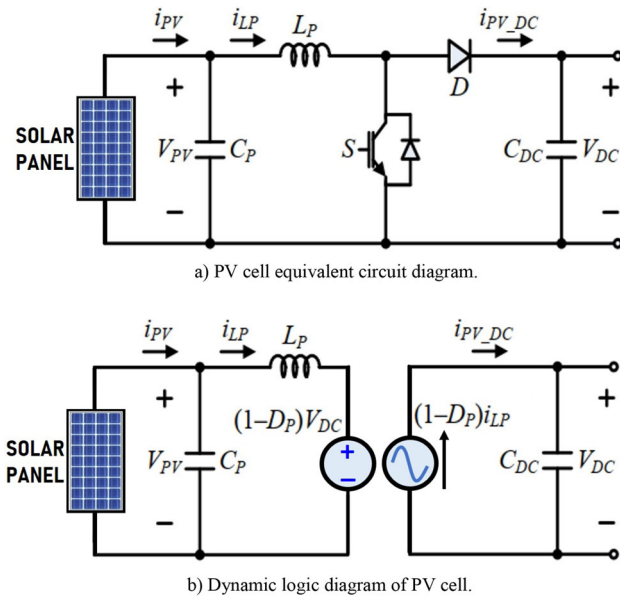
a) PV cell equivalent circuit diagram.

b) Dynamic logic diagram of PV cell.

Fig. 6 **a** PV cell equivalent circuit diagram. **b** Dynamic logic diagram of PV cell

i_{LP}; the accountable proportion from the DC-DC boost converter current is K_P.

3.4 Supercapacitor and AC-DC converter

The model circuit of the supercapacitor has shown in Fig. 6. In addition to taking into account the supercapacitor's self-applied-release phenomenon and Joule reduction, which are indicated by the aversion to R_{pSC} and R_{qSC}, respectively, the following depiction also takes these factors into account about the capacitor C_{SC}. As per Fig. 7, the associated dynamic computations of the supercapacitor employed were represented as:

$$(SC_c)P_w = C_{SC}V_{CSC} \tag{11}$$

$$V_{SC} = V_{CSC} + I_{SC}R_{sSC} \tag{12}$$

where V_{CSC} is the voltage across C_{SC} and V_{SC} and I_{SC} are the voltage and current of the supercapacitor, respectively.
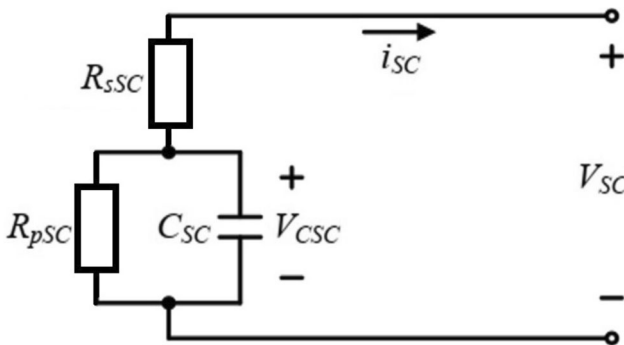
Fig. 7 A supercapacitor's equivalent circuit

The streamlined design of the employed schemes is shown in Fig. 8(a). The converter consists of a power-storing inductor L_S and two switches, S_1 and S_2, that are regulated in a subsidiary method. This specific configuration allows the converter's feature of two-way current flowing. In the buck setting method, the current travels to the supercapacitor through the DC connection, where switch S_1 acting as a switch and S_2 as a diode (Hannan et al. 2019). However, in the procedure's boost setting, S_2 functions as a switch and S_1 as a diode, with the supercapacitor providing the energy to the DC connection. For instance, the full transitional processes are sometimes disregarded when the DC-DC converter is built in a supercharging condition. The dynamic average -value of the bidirectional DC-DC improved topology with exceptional function and the step-down setting approach are
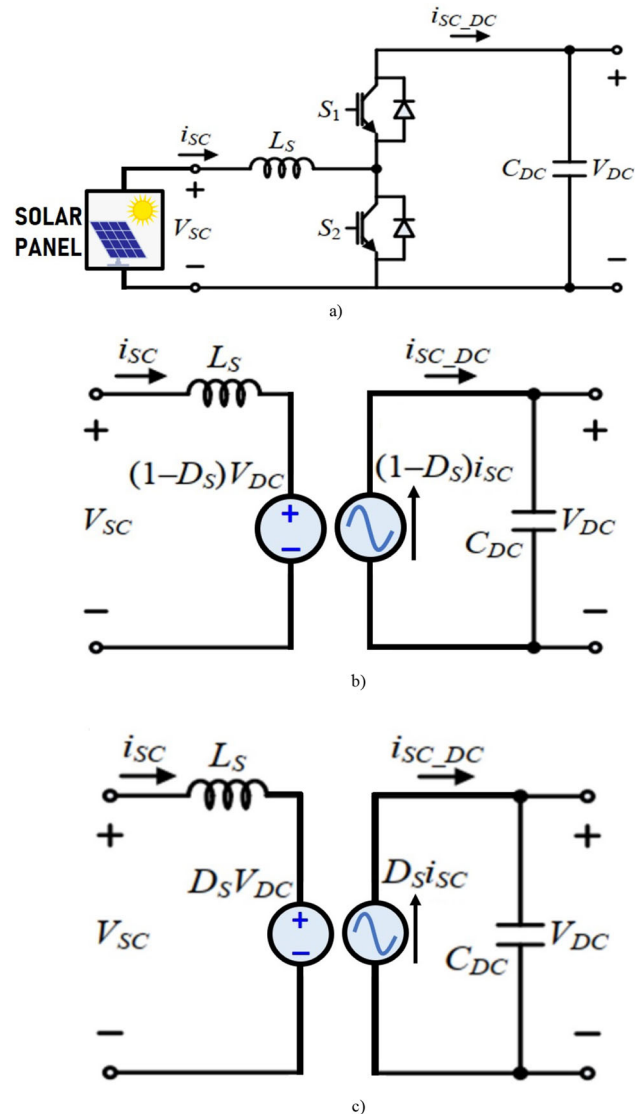

a)

b)

c)

Fig. 8 **a**, **b**, **c** Back-to-back DC-DC converter basic diagrams

displayed in Figs. 8(b) and (c), respectively. The topology's mathematical expression is provided below:

4 (a) Boost mode:

$$(L_s)p(i_{sc}) = -R_s i_{sc} + V_{sc} - (1 - D_s)V_{DC} \tag{13}$$

$$i_{SC-DC} = (1 - D_s)i_{sc} \tag{14}$$

5 (b) Buck mode:

$$(L_s)p(i_{sc}) = -R_s i_{sc} + V_{sc} - D_s V_{DC} \tag{15}$$

$$i_{SC-DC} = D_s i_{sc} \tag{16}$$

In this case, i_{SC-DC} represents the specific power in the DC-link portion, and L_s and R_s would be the inductance and resistance of the power-storing inductor respectively.

5.1 Modelling of FLC-controlled PWM inverter

The proposed system utilizes a fuzzy logic-controlled PWM inverter to provide balanced power supply. The Fuzzy logic-controlled inverter is connected to the PV-wind-battery storage system (Jan et al. 2021) and is employed to regulate the output voltage to a specified level. This is achieved by utilizing two fuzzy inputs, namely errors (E) and change of error (COE). The fuzzy rule matrix, based on the "if and then rule," is presented in Table 2 according to the study conducted by (Lii et al. 2004). The proposed control strategy involves the utilization of fuzzy control to generate the desired gate pulse for the PWM inverter. The MAMDANI fuzzy interface is utilized for the development of 49 rule bases. These rule bases are then applied to a PWM inverter in order to generate the desired gate pulse.

Table 2 Rule base FLC

e / de	MN	SN	NE	SP	MP	LN	LP
MN	LP	MP	MP	NE	NE	LP	EZ
SN	LP	SP	SP	MN	SN	LP	MN
NE	MP	SP	NE	SN	MN	LP	LN
SP	SP	SP	SN	SN	NL	MN	LN
MP	NE	NE	MN	MN	LN	NE	LN
LN	LP	LP	LP	NE	NE	LP	NE
LP	NE	NE	LN	LN	LN	NE	LN

Where Large Positive (LP), Medium Positive (MP), Small Positive (SP), Negligible Error (NE), Small Negative (SN), Large Negative (LN), Medium Negative (MN).

The fuzzy controller regulates the 4 kHz gate pulse and provides six gate signals to PWM inverter to generate the desired output.

5.2 Arrangement of voltage source inverter

Figure 1 shows a voltage source inverter with an LC filter, a net-worked line, and a boost transformer for grid power computation (Jan et al. 2021). All these kinds of elements' specific dynamic units can be stated as follows (Hannan et al. 2019; Mosaad et al. 2019b):

$$(L_I)p(i_{dI}) = -R_I i_{dI} + \omega_e L_I i_{qI} + v_{dI} - v_{dPCC} \tag{17}$$

$$(L_I)p(i_{qI}) = -R_I i_{qI} - \omega_e L_I i_{dI} + v_{qI} - v_{qPCC} \tag{18}$$

$$(C_I)p(v_{dPCC}) = i_{dI} - i_{dTL} + \omega_e C_I v_{qPCC} \tag{19}$$

$$(C_I)p(v_{qPCC}) = i_{qI} - i_{qTL} - \omega_e C_I v_{dPCC} \tag{20}$$

$$(L_{TL})p(i_{dTL}) = -R_{TL} i_{dTL} + \omega_e L_{TL} i_{qTL} + v_{dPCC} - v_{dinf} \tag{21}$$

$$(L_{TL})p(i_{qTL}) = -R_{TL} i_{qTL} - \omega_e L_{TL} i_{dTL} + v_{qPCC} - v_{qinf} \tag{22}$$

where the voltage and currents of the VSI are (v_{dI} and v_{qI}) and (i_{dI} and i_{qI}); the voltages (v_{dPCC} along with v_{qPCC}) and (v_{dinf} along with v_{qinf}) are measured at the same level of the PCC; and the energies of the interlinking range are typically indicated as (i_{dTL} and i_{qTL}).

5.3 Superconducting fault current limiter

The SFCL system, as proposed by (Dhara et al. 2019a), can effectively alleviate system disturbances caused by faults through the introduction of regulated voltage across an injecting transformer. The proposed system is tested during different types of disturbances like single line-to-ground fault (L-G), double line-to-ground fault (L-L-G), triple line-to-ground fault (L-L-L-G) fault and voltage sag/swell conditions. The process of SFCL via a flow chart is given in Fig. 10.

5.4 Battery storage energy system

The BS controller's primary function is to regulate the power mode of traditional load based on the grid and battery's operational state. The BS will be able to perform various operations independently along with fulfilling the demand side load power Laha et al. (2018). in this section, to focus on the power frequency management (PFM)
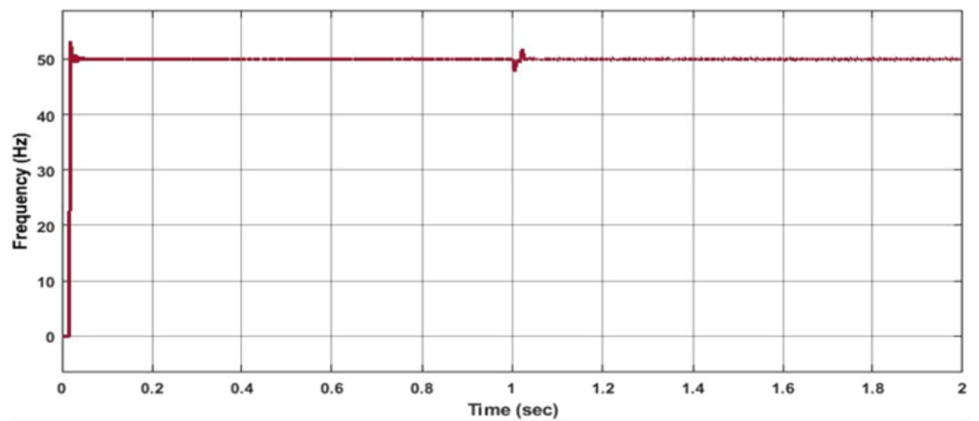
Fig. 9 Lithium-ion battery cycle life vs. DOD
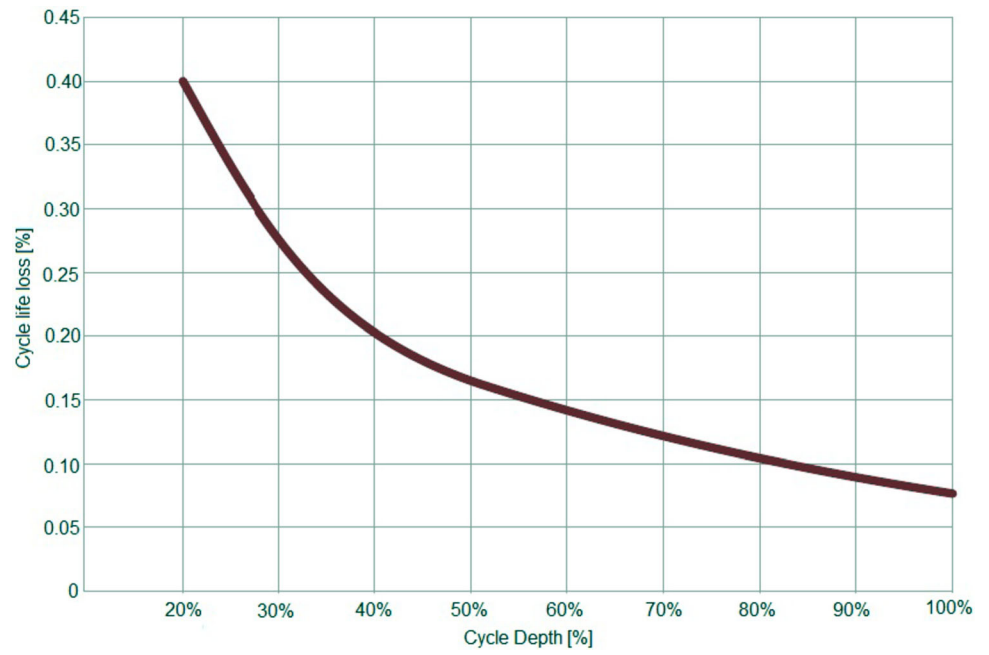
Fig. 10 Simulation response of SOC
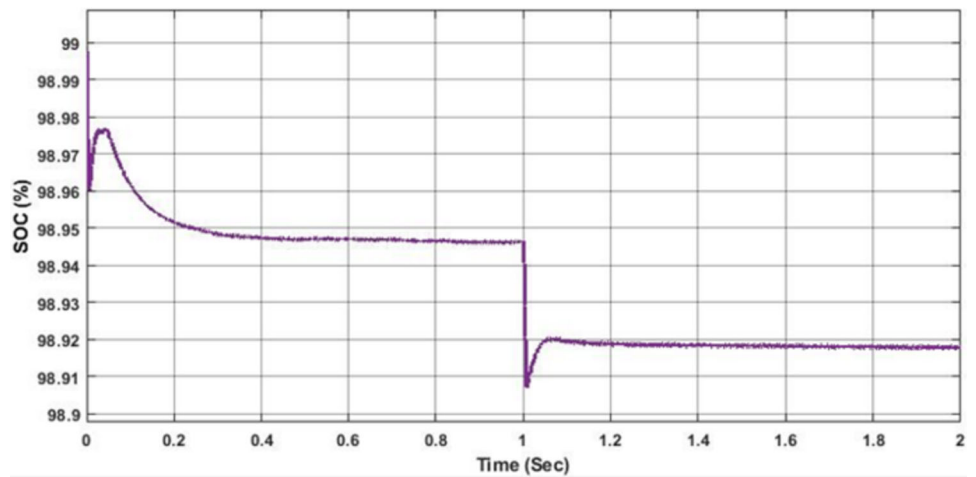
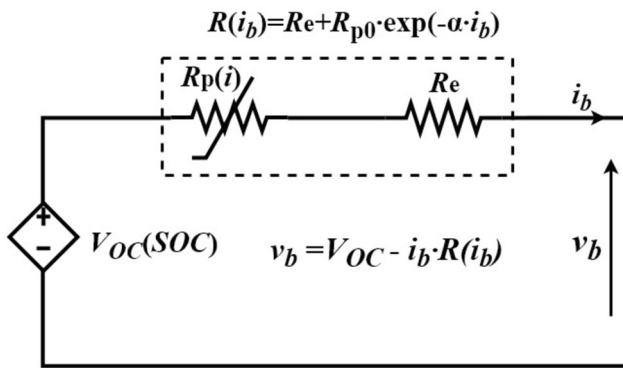**Fig. 11** Simulation response for frequency deviation

$$R(i_b) = R_e + R_{p0} \cdot \exp(-\alpha \cdot i_b)$$

Fig. 12 Simulation circuit model of battery loss assessment

function, which will be discussed in depth later (Mosaad et al. 2019f).

In battery mode, the battery's power can be characterized as follows:

$$G_P = L_P + B_P. \tag{23}$$

Where G_P the grid is power, L_P is the load power and B_P is the BS controller's battery power consumption. As a result, grid power may be stated in the following way,

$$G_p = L_P + B_P + C_P. \tag{24}$$

Hence C_P is the BS controller power consumption. During charging, discharging, and energy storage, the battery will lose power and energy. The type of battery used and how it is utilized have an impact on the total loss.

6 Power frequency management (PFM) modeling

6.1 Power frequency management with battery power control

The primary purpose of battery power control in this paper is to implement at load-side PFM. While doing so, we want to maintain a specific state of charge (SOC) for the battery, for example, 75% of its original capacity. As a result, the battery power B_P is divided into two elements Mosaad et al. (2019f) for SOC compensation, reliant element on line frequency $B_{Pf}(\Delta f)$ and battery SOC compensation offset element $P_{Bs}(SOC)$ as,

$$B_P = B_{Pf}(\Delta f) + B_{PS}(SOC). \tag{25}$$

Therefore, the grid power in (2) becomes,

$$G_P = L_P + \left[B_{Pf}(\Delta f) + B_{PS}(SOC)\right] + C_P. \tag{26}$$

It is also important to note that the battery can only transfer energy to the connected load and not return to the grid.

The response among standard battery systematic life-cycle loss and depth of discharge (DOD), including lifecycle loss growing with lifecycle depth are represented in Fig. 9.

6.2 Assessment of battery energy loss

The method for estimating the amount of battery energy loss during PFM operation is proposed in this section. If the SOC is preserved this energy dissipation may be calculated, that is, if the SOC values at the start and end of a particular running period are the same as each other. To put it another way, SOC set is set to the value of SOC. The consequence will be a reversal of any fluctuation in SOC induced by power factor correction (PFC) regulation, with offset power matching the regulation direction, returning the SOC to its starting value. Because of the way that based on the path of the frequency deviation the regulating power ΔB_f can be either + ve or –ve and according to the SOC variation ΔB_s can be either + ve or –ve. In this way, the connected battery energy exchange, denoted by the symbol ΔB_E, might be computed as

$$\Delta B_E = \Delta B_f + \Delta B_s. \tag{27}$$

Where ΔB_f and ΔB_s are the exchange energy, the main frequency regulation and SOC compensation must be implemented.

A simulation of the state of charge of the battery being used is performed using one-day realistic frequency data. To simulate the SOC, the coulomb counting approach is utilized. Hence, during operation 0.017 Hz is adjusted for PFC's dead-band frequency, whereas 0.04 Hz is adjusted for droop frequency. SOC is started with a value of 50%. The frequency deviation for reality and the simulated SOC are exhibited in Figs. 10 and 11 respectively.

The energy loss is modeled using a battery energy efficiency model from previous research Pinzon et al. (2019). The model uses a current-dependent nonlinear resistance to represent the entire energy generated by activation, awareness and ohmic polarization as illustrated by the equation below.

$$V_{OC}(SOC) = [R_P(i) + R_e]i_b. \tag{27}$$

where $R_P(i)$ and R_e are experimentally determined model parameters. The analogous circuit prototype of the battery is depicted in Fig. 12. The battery open circuit voltage is represented by V_{OC} in the circuit model.

6.3 Renewable energy generation limitations

To maintain the PV and wind generator (WG) outputs at their respective "t" time intervals under the following minimum and maximum power restrictions (Zhao et al.
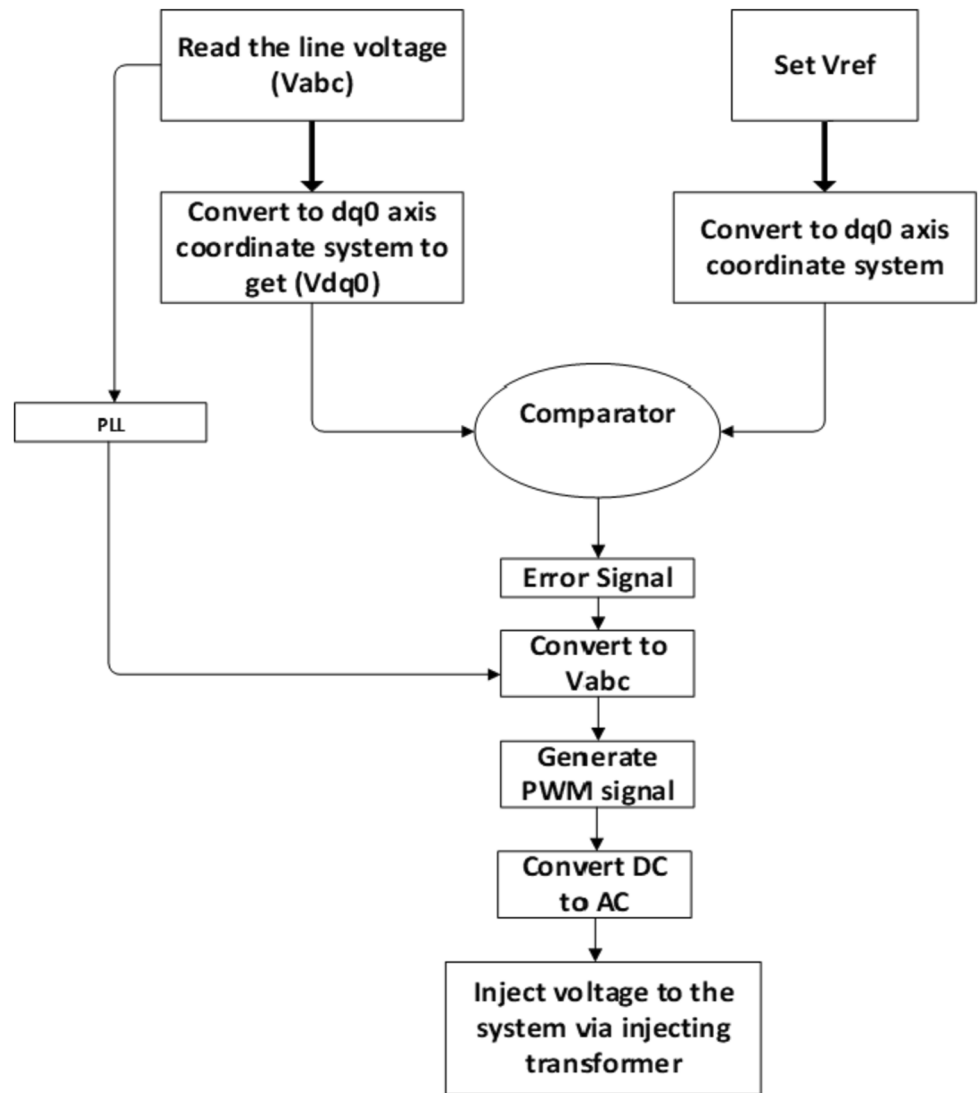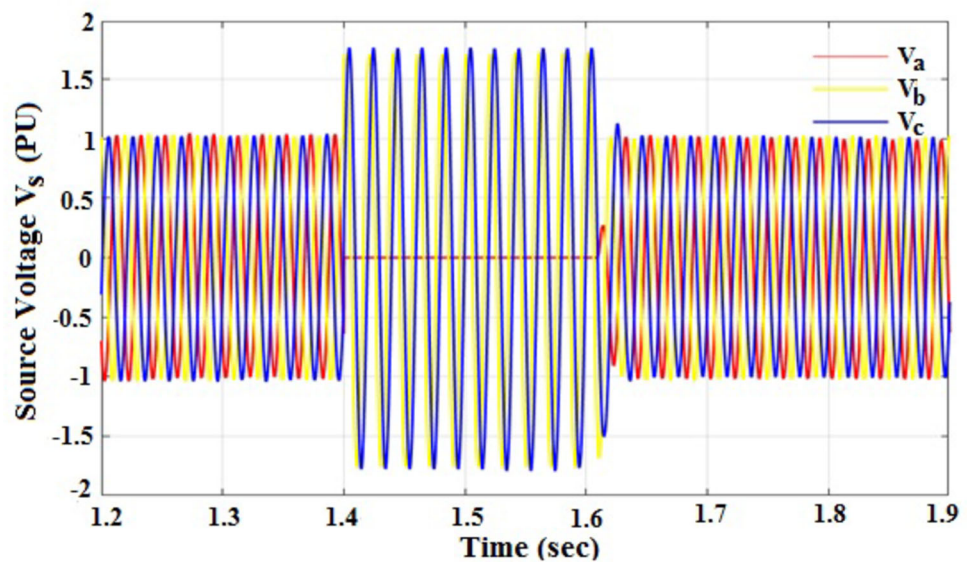
Fig. 13 Flow diagram operation of SFCL

```
┌──────────────────┐                          ┌──────────────┐
│ Read the line     │                         │   Set Vref   │
│ voltage (Vabc)    │                         │              │
└──────────────────┘                          └──────────────┘
        │                                            │
        ▼                                            ▼
┌──────────────────┐                      ┌──────────────────────┐
│ Convert to dq0    │                      │ Convert to dq0 axis  │
│ axis coordinate   │                      │ coordinate system    │
│ system to get     │                      │                      │
│ (Vdq0)            │                      └──────────────────────┘
└──────────────────┘                                 │
        │                                            │
        │          ┌───────────────────┐             │
        └─────────▶│    Comparator     │◀────────────┘
  ┌─────┐          └───────────────────┘
  │ PLL │                    │
  └─────┘                    ▼
    │              ┌──────────────────┐
    │              │   Error Signal   │
    │              └──────────────────┘
    │                       │
    │                       ▼
    │              ┌──────────────────┐
    └─────────────▶│ Convert to Vabc  │
                   └──────────────────┘
                            │
                            ▼
                   ┌──────────────────┐
                   │ Generate PWM     │
                   │ signal           │
                   └──────────────────┘
                            │
                            ▼
                   ┌──────────────────┐
                   │ Convert DC to AC │
                   └──────────────────┘
                            │
                            ▼
                   ┌──────────────────────┐
                   │ Inject voltage to    │
                   │ the system via       │
                   │ injecting transformer│
                   └──────────────────────┘
```

Fig. 14 Source voltage behaviour at an L-G fault instant

Fig. 15 SFCL injected voltage at phase A during L-G fault
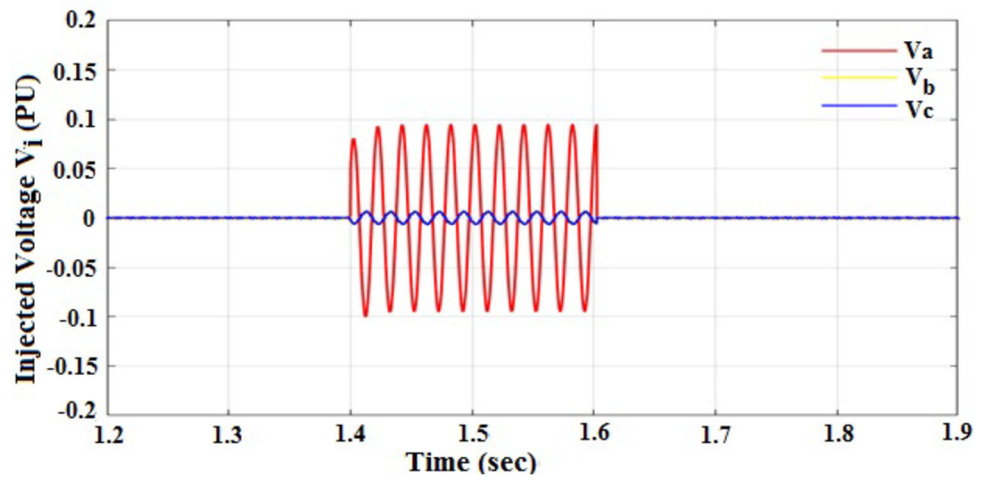
Fig. 16 Load voltage response throughout L-G fault
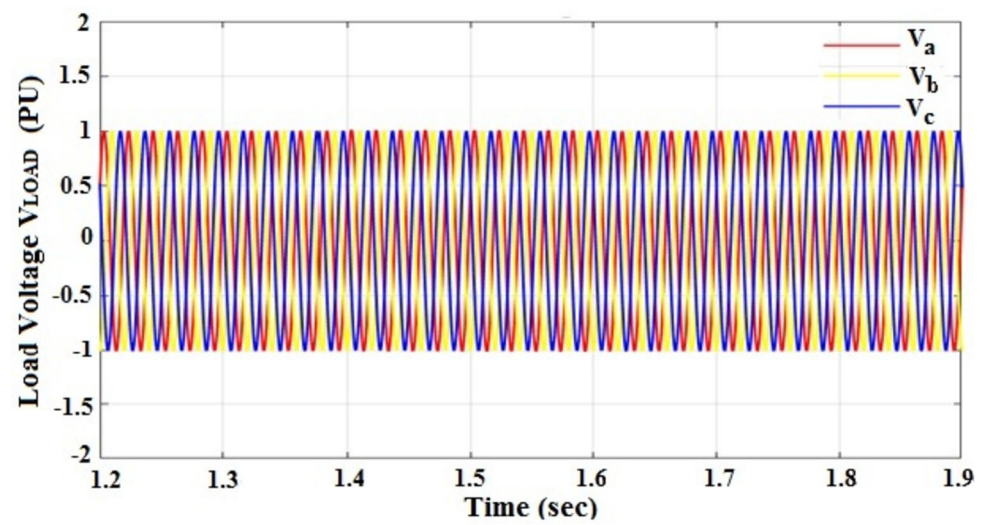
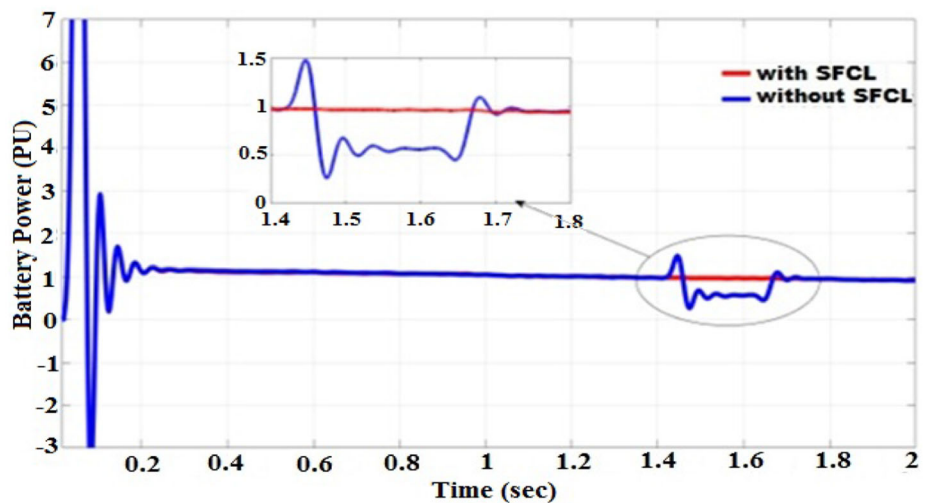
Fig. 17 Voltage profile during L-G fault
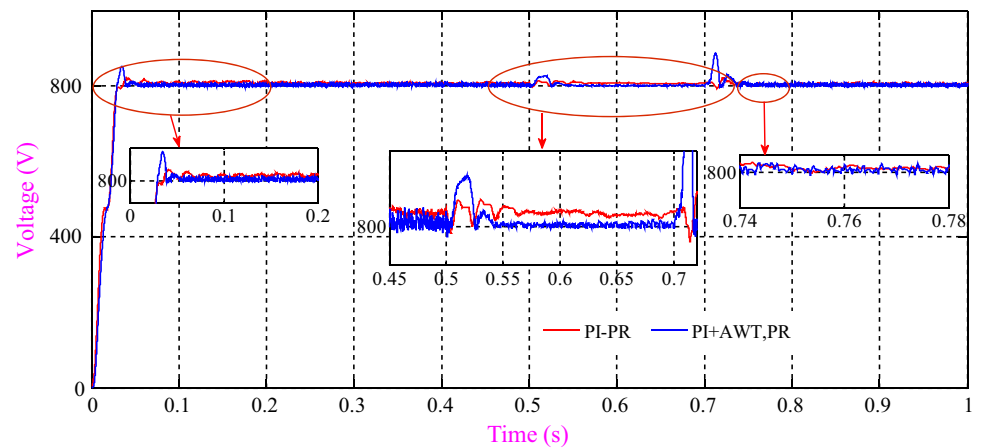
Fig. 18 a Behavior of battery
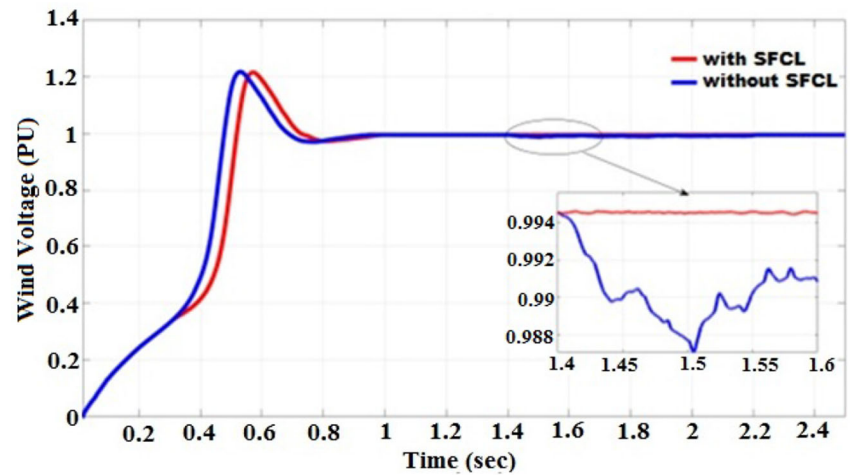system voltage during 3-phase
fault with and without SFCL.
b Behavior of battery system
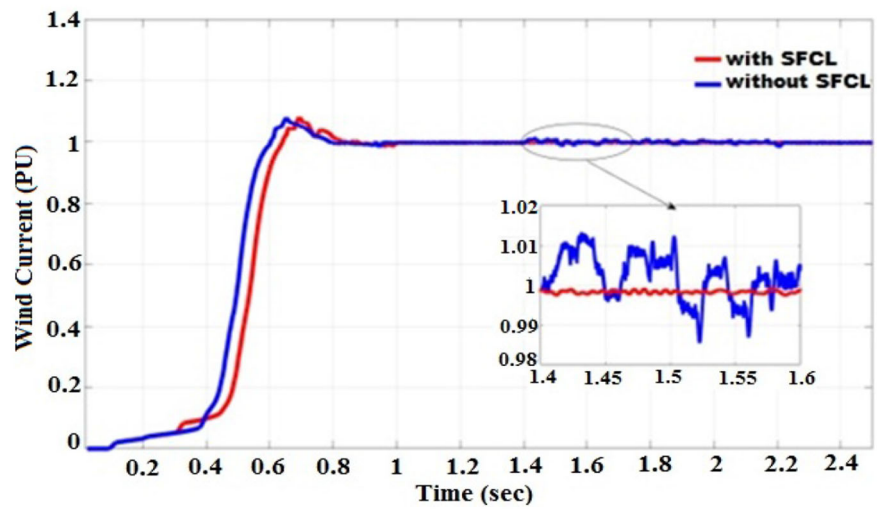current during 3-phase fault
with and without SFCL.
c Behavior of battery system
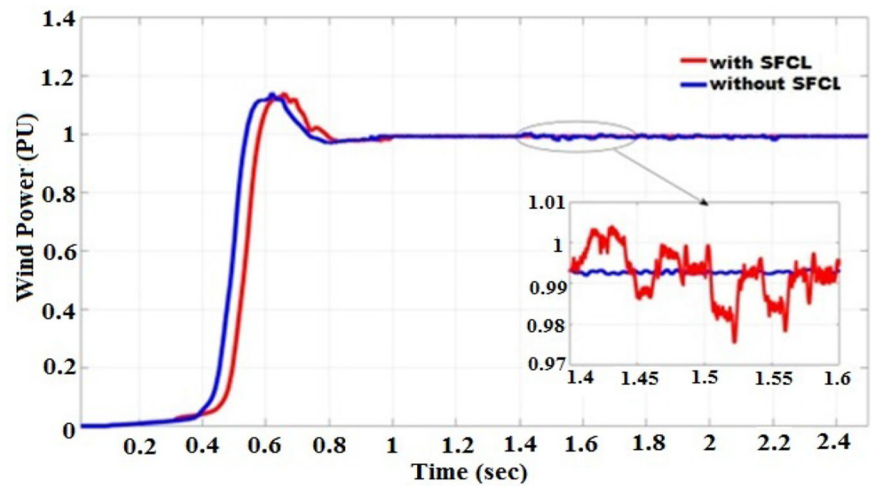power during 3-phase fault with
and without SFCL
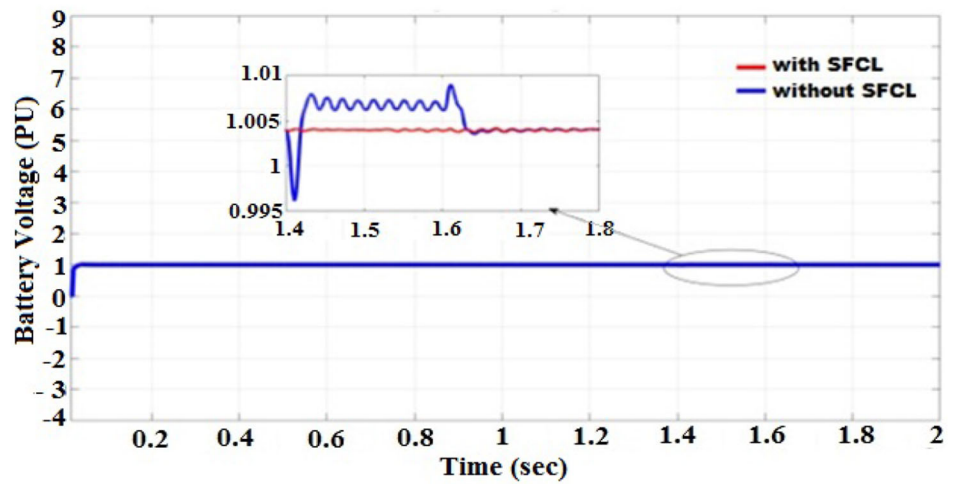
a) Behavior of battery system voltage during 3-phase fault with and without SFCL.
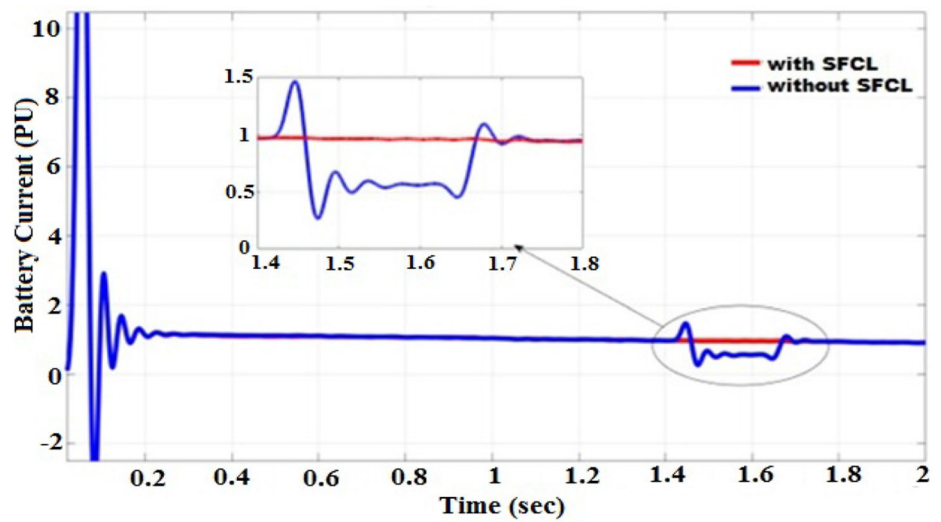
b) Behavior of battery system current during 3-phase fault with and without SFCL.

c) Behavior of battery system power during 3-phase fault with and without SFCL.

a) WECS voltage during 3-phase fault with and without SFCL.

b) WECS current during 3-phase fault with and without SFCL.

c) WECS power during 3-phase fault with and without SFCL.

Fig. 20 **a** PV system power with and without SFCL. **b** PV system current with and without SFCL. **c** PV system voltage with and without SFCL
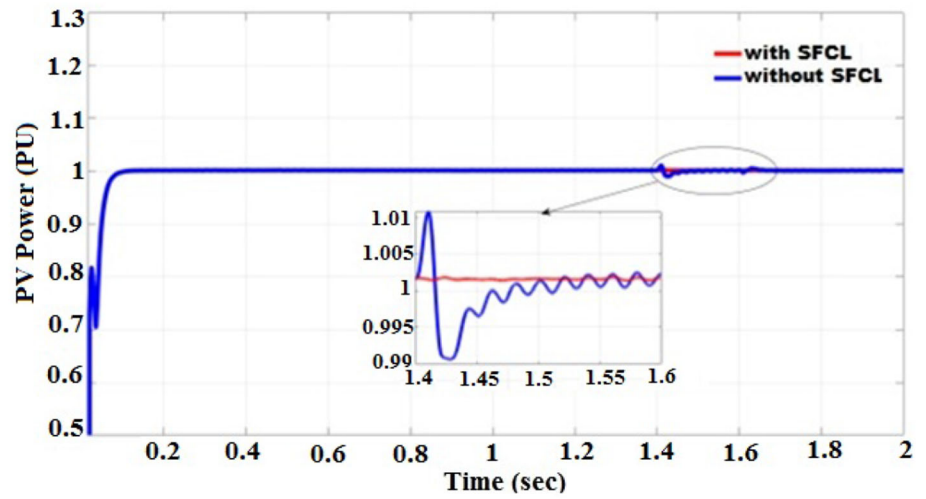
a) PV system power with and without SFCL.
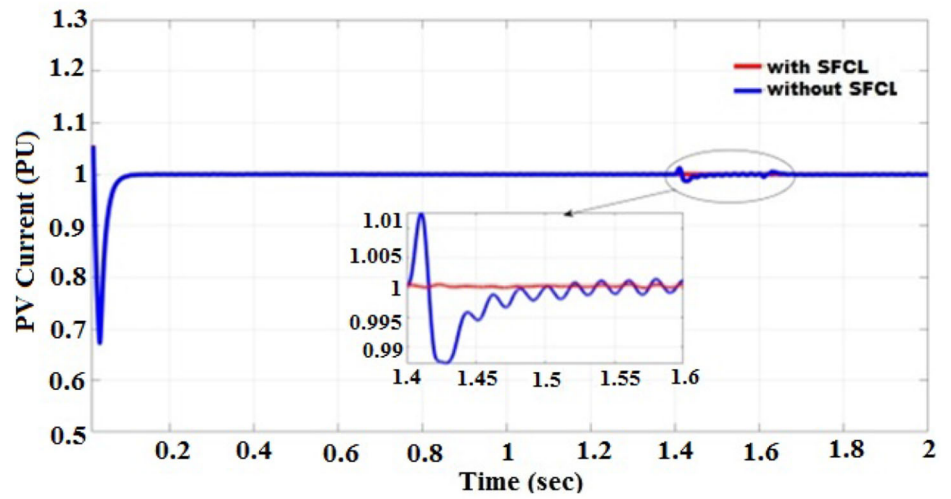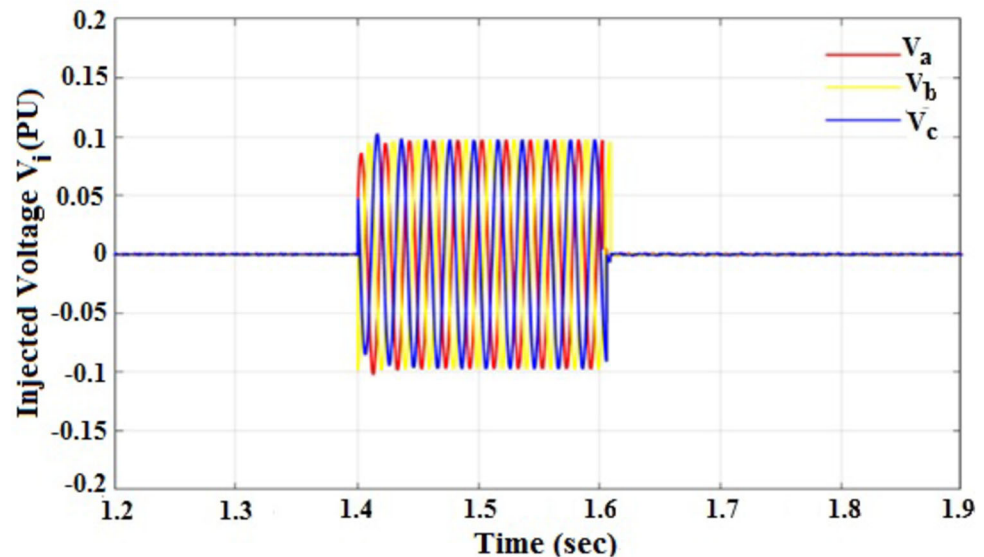

b) PV system current with and without SFCL.
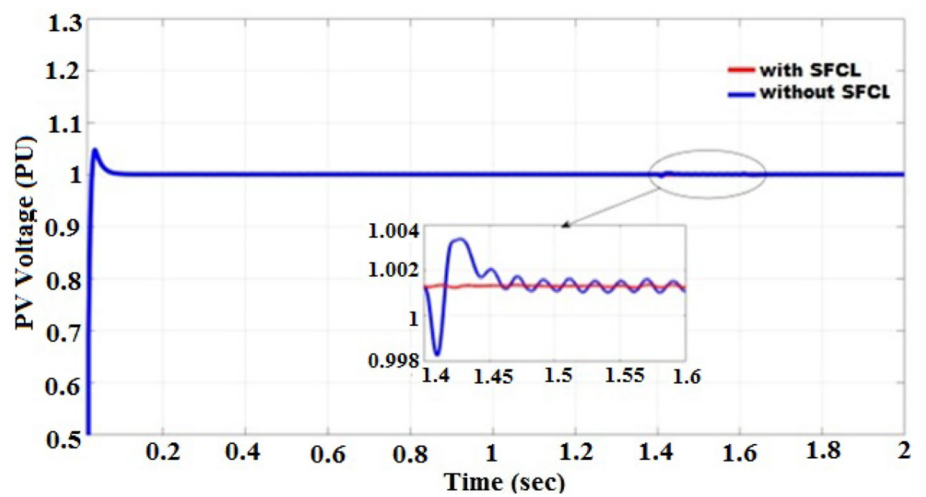
c) PV system voltage with and without SFCL.

Fig. 21 Source behavior between three-phase faults
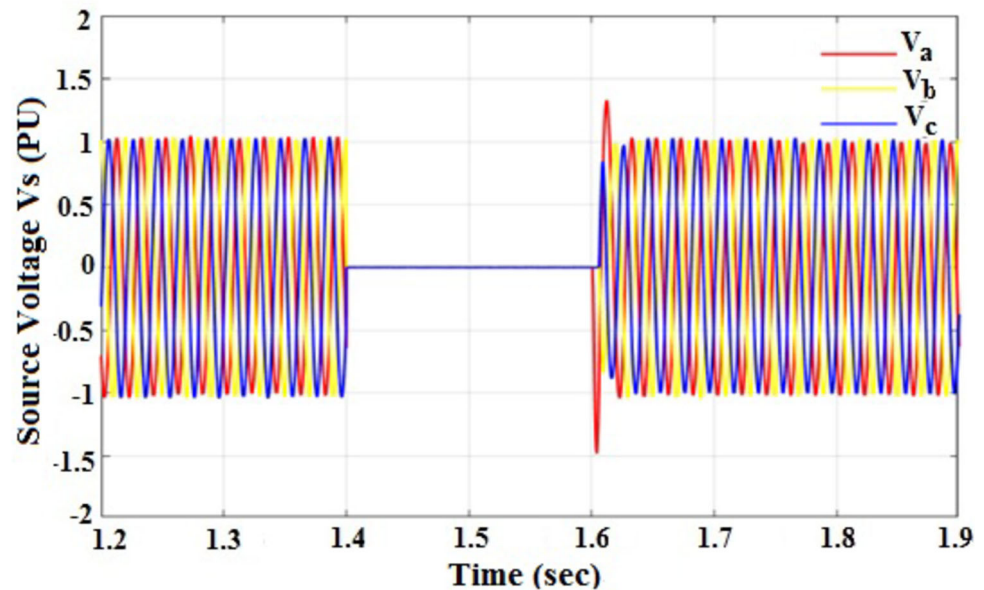
Fig. 22 Injected voltage during three-phase faults

(2010), they must be kept at their respective "t" time intervals within the following minimum and maximum power limits.

$$P_{PV,min} \leq P_{PV}(t) \leq P_{PV,max}, \quad (29)$$

$$P_{WG,min} \leq P_{WG}(t) \leq P_{WG,max}. \quad (30)$$

Where $P_{PV,min}$ and $P_{PV,max}$ are the minimum and maximum power constraints imposed by each PV module. $P_{WG,min}$ and $P_{WG,max}$ are the power constraints imposed by each WG at the lowest and highest levels (Praiselin et al. 2017; Zho 2010).

6.4 Limitations of battery powers

The battery voltage still has to be below the specified power limit, which can be expressed as (Kim et al. 2013; Li et al. 2018):

$$P_{BSch,top} < P_{BS}(t) < P_{BSdch,bottom}. \quad (31)$$

Where $P_{BSch,top}$ and $P_{BSdch,bottom}$ are the maximum charging and discharging powers of the battery, respectively. Always ensure that the battery's energy storage capacity is between the minimum and maximum limits:

$$E_{BS,lowest} < E_{BS}(t) < E_{BS,highest}. \quad (32)$$

Fig. 23 Load voltage during three-phase faults
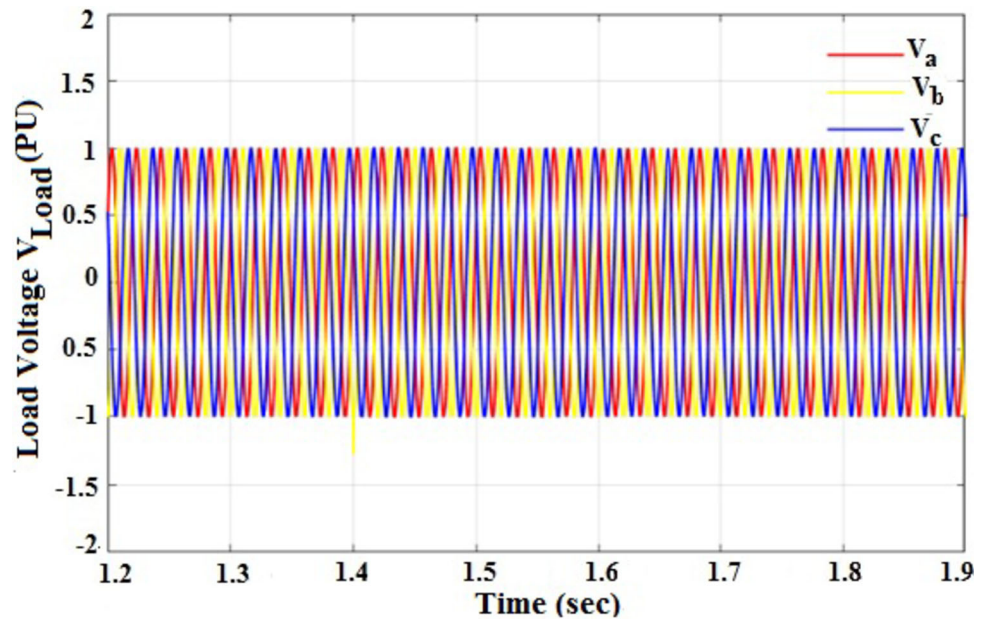
Fig. 24 Wind power under fluctuating wind velocity
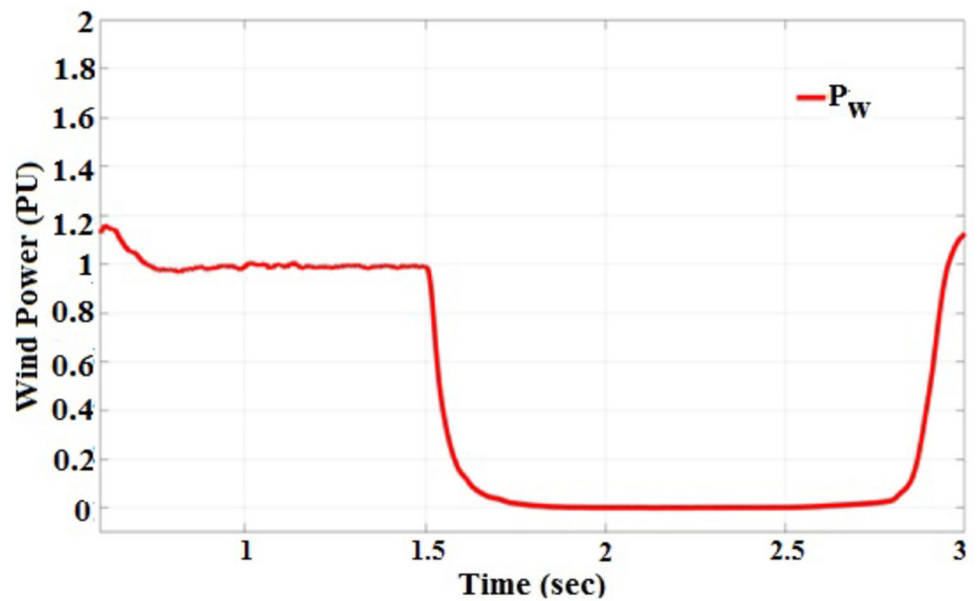
Where $E_{BS,lowest}$ and $E_{BS,highest}$ are respectively, the lowest and maximum energy limitations for batteries. Battery SOC levels should be kept as low as possible as a result of this consideration:

$$SOC_{lowest} < SOC(t) < SOC_{highest}. \tag{33}$$

7 Results and discussion

The mentioned system performance is tested under different faults and voltage sag/swell conditions. During test conditions I and II, different faults are applied at the PCC of the bus for 100 ms. In test condition III variable, wind velocity and solar irradiation is applied to the system. Test condition IV presents the harmonic distortion under non-linear load conditions. The asymmetrical and symmetrical conditions produce voltage sag/swell in the system voltage.
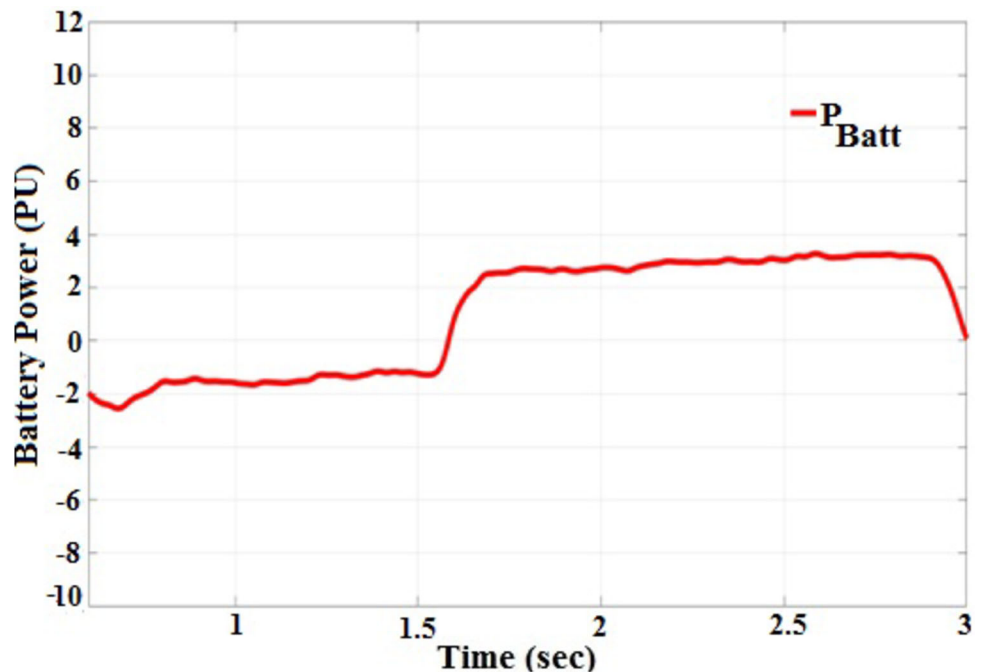
7.1 Test condition I: single line to ground fault (L-G) at point of common coupling (PCC) bus F_1

The L-G fault is introduced to the F_1 feeder at intervals of 1.4 to 1.6 s throughout this test. This defect affects the output of many producing sources; phase A of a three-

Fig. 25 Constant PV power under fluctuating wind velocity
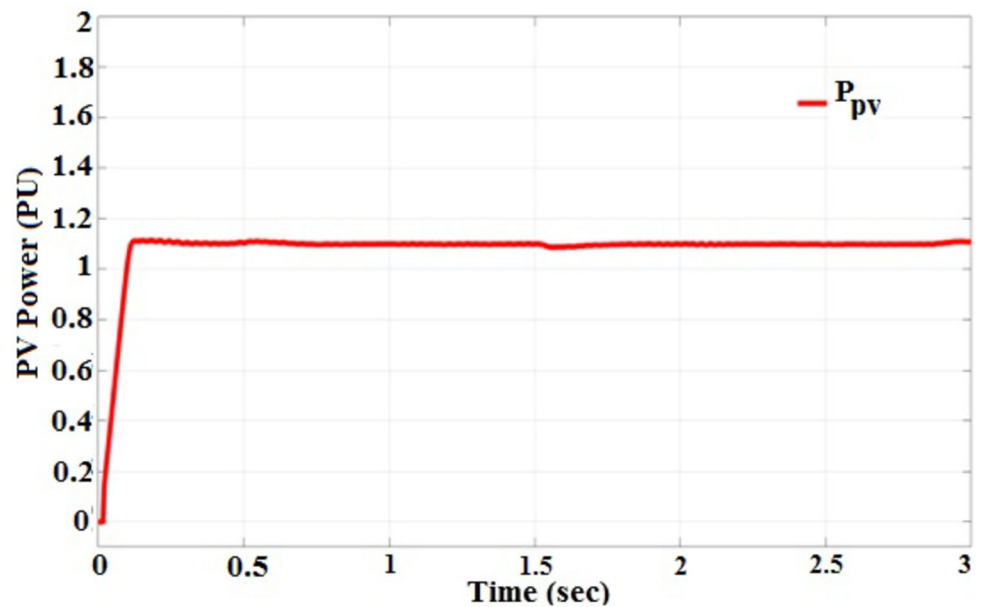
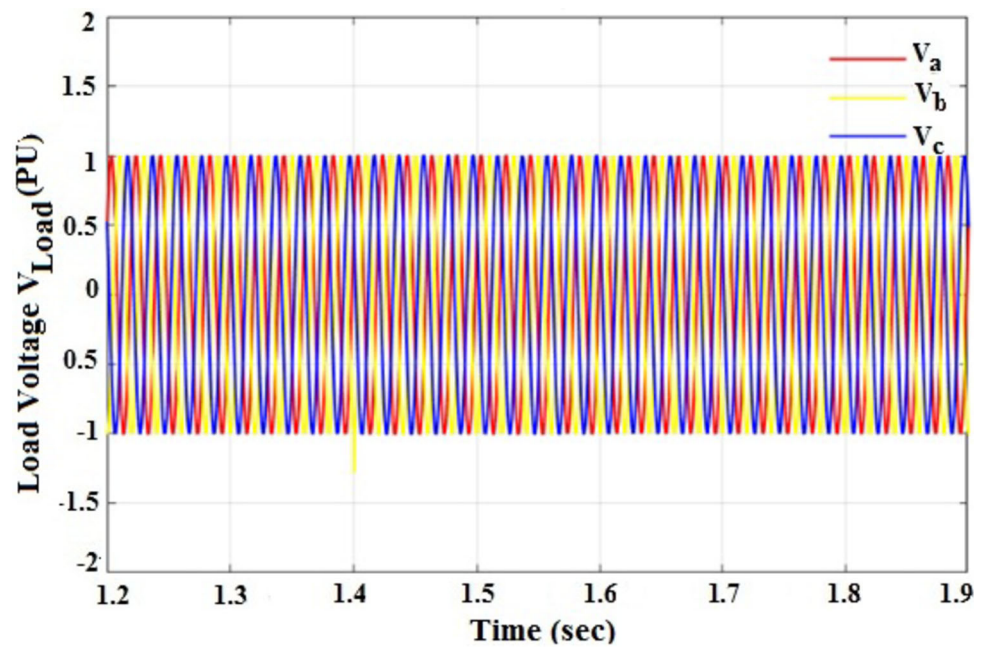**Fig. 26** Battery power under fluctuating wind velocity

phase supply is connected to the ground, therefore the voltage of phase A becomes zero, while the voltage of phases B and C increases in this interval, as illustrated in Fig. 13 flow diagram.

The SFCL inject voltage for Phase A during fault (Katarzyński and Olesz 2020) and FLC restrict the voltage within the desired magnitude to make the load voltage constant as shown in Fig. 14 and 15 correspondingly. Also, throughout the L-G fault, the constant load voltage is displayed in Fig. 16.

The voltage profile during L-G fault is illustrated in Fig. 17, which shows the transient states during a short circuit. The transient is occurred for the time span between (0–0.2) sec, (0.45–0.7) sec and (0.74–0.78) sec. Specifically, the transient states are shown by zooming the first few cycles of the entire time span during L-G fault.

Fig. 27 Load voltage under fluctuating wind velocity

Fig. 28 PV power under fluctuating solar irradiation
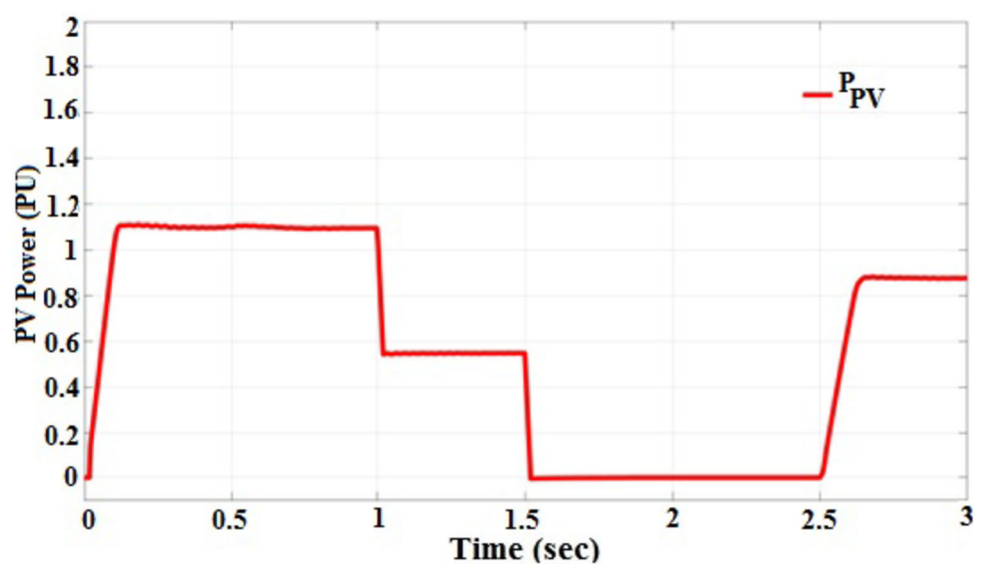
## 7.2 Test condition II: three-phase faults at PCC bus F_2

The PV, wind, and battery systems' power, voltage, and current are unaffected during this fault occurrence. The behaviors of BESS during three-phase faults with and without SFCL are shown in Fig. 18: a, b and c respectively. The voltage of the battery drops as the current of the battery grows. The battery might be disconnected from the hybrid system if its current rises at a rapid rate (Osama abed et al. (2018).

Figures 19 and 20 a, b, c are depicts the behavior of WECS and PV systems, respectively Rehman et al. (2021).

As seen in Fig. 13 the fault causes an enhancement in the WECS current. During the fault period the performance of output voltage is superior with SFCL as compared to without SFCL, as shown in Fig. 19 a, b and c respectively. SFCL injected voltage at bus PCC with minimum harmonics and was also able to maintain the constant load voltage.

In the three-phase failures, as seen in Fig. 21, all phase voltages drop to zero. Figure 22 shows that the SFCL introduced the proper voltage magnitude between fault timespan of 1.4 to 1.5 s. Figure 23 shows that the load voltage remained steady throughout the three-phase fault.

Fig. 29 Constant wind power fluctuating solar irradiation
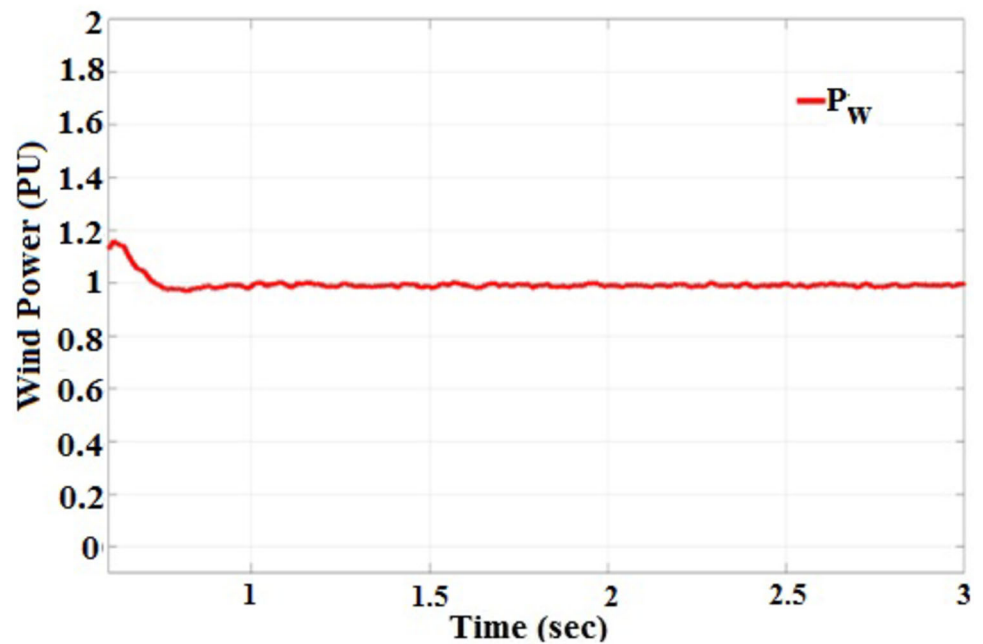
**Fig. 30** Battery power under fluctuating solar irradiation
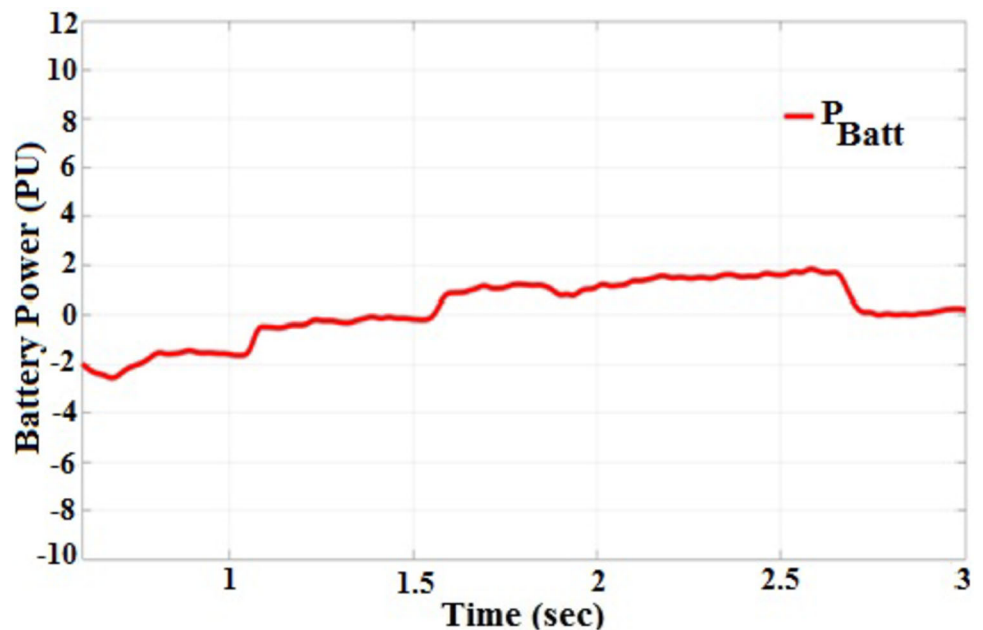
7.3 Test condition III: wind velocity variation with constant solar irradiation: -

During this test wind velocity varies from 12 m/s (at t = 0 to t = 1.5 s) to 6 m/s (at t = 1.5 s to t = 2.5 s) and then backwards to 12 m/s (at t ≈ 2.5 s), the solar irradiation is kept constant at 1000w/m^2 during this operation. The wind power during the operation is shown in Fig. 24. The PV power and battery power are shown in Figs. 25, 26, respectively.

According to Fig. 26 the present battery power balance is achieved by varying the wind speed. As seen in Fig. 27, the battery system compensated for the shortfall in power and maintained a constant load voltage throughout this brief period when solar alone was insufficient to provide the load requirement.

Fig. 31 Load voltage under fluctuating solar irradiation
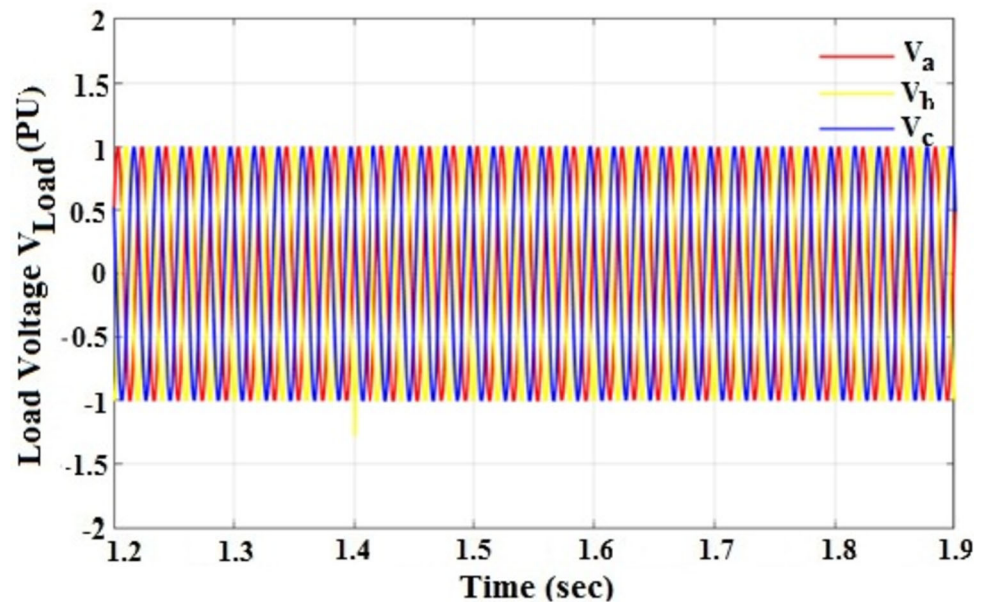
7.4 Test condition IV: solar irradiation varying with constant wind velocity

During this test irradiation varies from 1000 w/m^2 (at $t = 0$ to $t = 1.0$ s) to 500 w/m^2 (at $t = 1.0$ s to $t = 1.5$ s) and 0 w/m^2 (at $t = 1.5$ s to $t = 2.5$ s) and then 800 w/m^2(at $t = 2.5$ s to $t = 3.0$ s), the wind velocity is kept constant at 12 m/s during this operation.

The output of the photovoltaic system during operation is seen in Fig. 28. Additionally, Figs. 29 and 30 are depicting wind energy and battery energy, respectively.

7.5 Test condition V: power electronics loads

Switching power supply, variable speed drives, solid-state controllers, and other sensitive electronic equipment create significant harmonics and nonlinear loads. Voltage distortion, a poor power factor (PF), and stress on supply power system equipment are all caused by harmonics in these non-linear loads. Harmonics from no sinusoidal loads has an impact on the electrical microgrids impedance. Figure 31 shows that an FLC inverter-SFCL-BS combo may meet IEEE 519 standards for eliminating harmonic distortion and voltage sag (Shrivastav et al. (2019).

Figures 32 a, b) are shows the THD analysis for the system without and with SFCL. The THD of the proposed system is lesser with SFCL at 0.87% in comparison to 1.43% without using SFCL. Table 2 shows a comparison of different existing techniques. The modulation was generally done using two or three-level inverters. In terms of harmonic reduction, power factor, switching mechanisms,

and hardware requirements, Table 3 compares the performance of the proposed developed inverter controller to that of other existing systems.

8 Conclusions

The fuzzy controlled inverter and SFCL in photovoltaic (PV)/wind hybrid microgrid systems have the ability to mitigate the negative impact caused by fault events such as phase faults at the PCC, unbalanced operation, and voltage swell/sag. The battery system functions as a supplementary power source for the load in situations where the hybrid system's power generation is unable to meet the load's power requirements. The rate of battery energy depletion is primarily influenced by the point at which the battery reaches its end of life and starts to experience degradation. Based on the results of the simulation, it is observed that the utilization of a dead band instead of a dead band loss results in a lower energy consumption in the battery. For example, when the dead-band is increased to 0.036 Hz, there is a reduction in energy loss due to the switching of small charge-release energy with the battery. Furthermore, according to modelling studies, increasing the regulation charge-release current leads to a decrease in the droop constant, resulting in additional energy loss. Among other factors, the results could contribute to the evaluation of the battery's benefits in frequency management and the energy losses incurred during the load-release exchange in the power factor correction process. This evaluation would be done by comparing these factors with those of the

Fig. 32 **a** THD for the system without SFCL. **b** THD for the system with SFCL
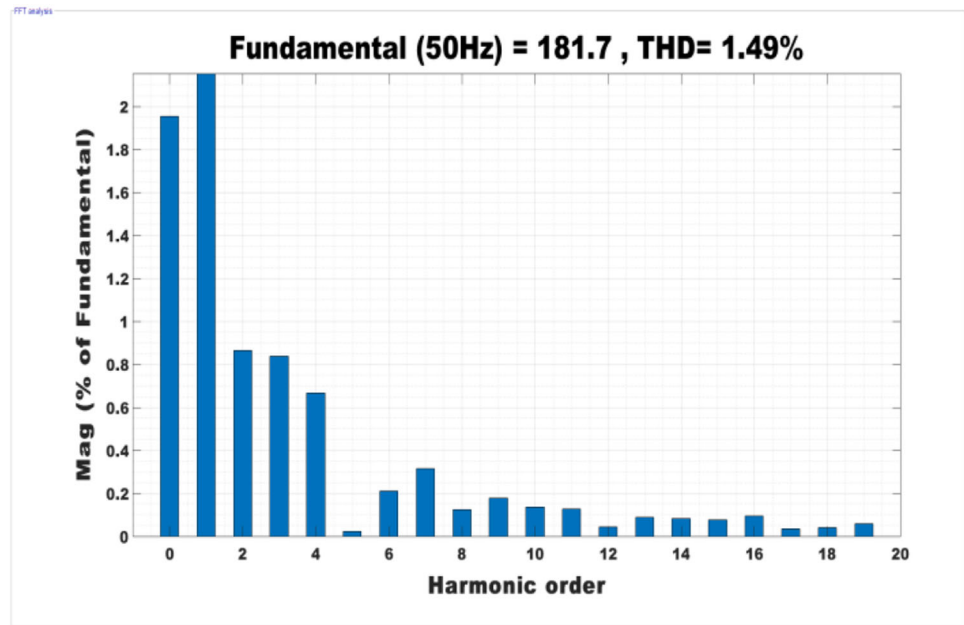
a) THD for the system without SFCL.
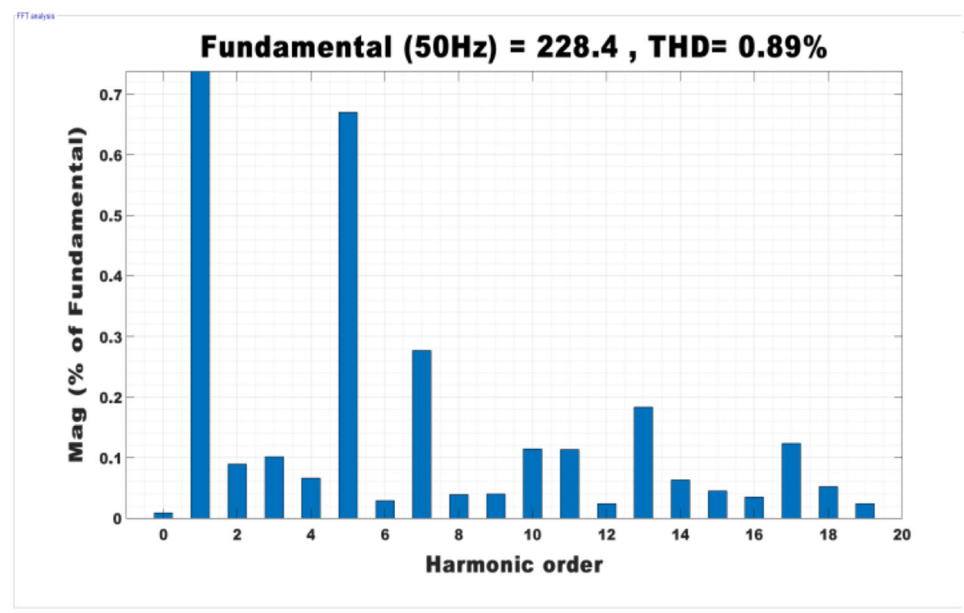
b) THD for the system with SFCL.

converters. The implemented control strategy effectively maintained the microgrid's continuous operation in the presence of abnormal conditions such as three-phase faults, higher power electronic load, and challenging scenarios of low insolation and wind speeds. The implemented control strategy effectively maintained the microgrid's uninterrupted operation in the presence of abnormal conditions such as three-phase faults, higher power electronics loads, and challenging scenarios with limited solar radiation and low wind speeds. The proposed SFCL offers several

benefits. It allows for voltage adjustment during faults, enables the variation of wind and photovoltaic (PV) generation, increases electronic load capacity, and ensures a uniform load voltage profile at the point of common coupling. The intelligent fuzzy logic controller based voltage source inverter regulates the voltage output to a specified level and minimizes the distortion of harmonics within the range specified in the IEEE 519 standard.

Table 3 Comparative analysis of converters

Reference key factor of converters	(Lii et al. 2004)	(Kanjiya et al. 2013)	(Aurangzeb et al. 2020)	(Zheng et al. 2018)	(Gee et al. March 2017)	(Jan et al. 2020)	(Mohomad et al. 2017)	Proposed Technique
Switching Topology	SVPWM	PWM	SPWM	SVPWM	SPWM	PWM	PWM	SFCL
Modulation Scheme	Simulink	Prog	Prog	Prog	Prog	Prog	Simulink	Simulink
Power Factor	Unity	Unity	–	–	0.9	0.87	–	Unity
THD	3.8	4.3	6.2	8.0	3.5	2.7	2.9	0.89
System Topology	3-phase 4-wire	1-phase 2-wire	1-phase 2-wire	1-phase 2-wire	3-phase 3-wire	3-phase 3-wire	3-phase 4-wire	3-phase 3-wire

References

Aurangzeb M, Xin A, Iqbal S, Jan MU (2020) An evaluation of flux-coupling type SFCL placement in hybrid grid system based on power quality risk index. IEEE Access 8:98800–98809. https://doi.org/10.1109/ACCESS.2020.2996583

BP statistical review of world energy. (2020) 69th ed

Dhara S, Sadhu PK, Shrivastav AK (2019a) Modelling and analysis of an efficient DC reactor type superconducting fault current limiter circuit. Rev Roum Sci Techn Électrotechn Et Énerg 64(3):205–210

Dhara S, Sadhu PK, Shrivastav AK (2022) Controlling of transient and harmonics using UPFC in an interconnected power grid. Microsyst Technol 28:2795–2805. https://doi.org/10.1007/s00542-022-05374-w

Dhara S, Shrivastav AK, Sadhu PK (2023) Radial basis function network based PV and wind system using maximum power point tracking. Microsyst Technol. https://doi.org/10.1007/s00542-023-05485-y

Abed El-Raouf MO, Mosaad MI, Mallawany A, Al-Ahmar MA, El Bendary FM (2018) "MPPT of PV-Wind-Fuel Cell of Off-Grid Hybrid System for a New Community Twentieth International Middle East Power Systems Conference (MEPCON), Cairo, Egypt, 2018, pp. 480-487. https://doi.org/10.1109/MEPCON.2018.8635165

Gee AM, Robinson F, Yuan W (2017) A superconducting magnetic energy storage-emulator/battery supported dynamic voltage restorer. IEEE Trans Energy Convers 32(1):55–64. https://doi.org/10.1109/TEC.2016.2609403

Gil-Antonio L, Saldivar B, Portillo-Rodríguez O, Ávila-Vilchis JC, Martínez-Rodríguez PR, Martínez-Méndez R (2019) Flatness-based control for the maximum power point tracking in a photovoltaic system. Energies 12(10):1843. https://doi.org/10.3390/en12101843

Hannan MA, Hossain Lipu MS, Ker PJ, Begum RA, Agelidis VG, Blaabjerg F (2019) Power electronics contribution to renewable energy conversion addressing emission reduction: Applications, issues, and recommendations. Appl Energy 251:113404. https://doi.org/10.1016/j.apenergy.2019.113404

Ibrahim AO, Nguyen TH, Lee D-C, Kim S-C (2011) A fault ride-through technique of DFIG wind turbine systems using dynamic voltage restorers. IEEE Trans Energy Convers 26(3):871–882. https://doi.org/10.1109/TEC.2011.2158102

Iqbal S, Xin A, Jan MU, Abdelbaky MA, Rehman HU, Salman S, Aurangzeb M, Rizvi SA, Shah NA (2020) Improvement of power converters performance by an efficient use of dead time compensation technique. Appl Sci 10(9):3121. https://doi.org/10.3390/app10093121

Jan MU, Xin A, Abdelbaky MA, Rehman HU, Iqbal S (2020) Adaptive and fuzzy PI controllers design for frequency regulation of isolated microgrid integrated with electric vehicles. IEEE Access 8:87621–87632. https://doi.org/10.1109/ACCESS.2020.2993178

Jan MU, Xin A, Rehman HU, Abdelbaky MA, Iqbal S, Aurangzeb M (2021) Frequency regulation of an isolated microgrid with electric vehicles and energy storage system integration using adaptive and model predictive controllers. IEEE Access 9:14958–14970. https://doi.org/10.1109/ACCESS.2021.3052797

Jou S, Lee S, Park Y, Lee K (2009) Direct power control of a dfig in wind turbines to improve dynamic responses". J Power Electr 9(5):781–790. https://doi.org/10.6113/JPE.2009.9.5.781

Jowder FAL (2009) Design and analysis of dynamic voltage restorer for deep voltage sag and harmonic compensation. IET Gener Transm Distrib 3(6):547–560. https://doi.org/10.1049/iet-gtd.2008.0531

Kanjiya P, Singh B, Chandra A, Al-Haddad K (2013) "SRF theory revisited" to control self-supported Dynamic Voltage Restorer (DVR) for unbalanced and nonlinear loads. IEEE Trans Ind Appl 49(5):2330–2340. https://doi.org/10.1109/TIA.2013.2261273

Katarzyński J, Olesz M (2020) Fault loop impedance measurement in circuits fed by UPS and principle of safety protection. Sustainability 12(23):10126. https://doi.org/10.3390/su122310126

Kim S-T, Kang B-K, Bae S-H, Park J-W (2013) Application of SMES and Grid Code compliance to wind/photovoltaic generation system. IEEE Trans Appl Supercond 23(3):5000804–5000804. https://doi.org/10.1109/TASC.2012.2232962

Laha SK, Sadhu PK, Ganguly A, Naskar AK (2018) Convergence tuning of solar power for enhanced energy harvesting. LAAR 48(2):113–118. https://doi.org/10.52292/j.laar.2018.268

Lan Y, Dai ST, Tao M, Yan XF (2018) Maximum power point tracking algorithm and computer aided design and analysis of direct drive doubly fed induction generator. Latin Am Appl Res 48(3):211–216. https://doi.org/10.52292/j.laar.2018.230

Li P, Xie L, Han J, Pang S, Li P (2018) A new voltage compensation philosophy for dynamic voltage restorer to mitigate voltage sags using three-phase voltage ellipse parameters. IEEE Trans Power Electron 33(2):1154–1166. https://doi.org/10.1109/TPEL.2017.2676681

Lii G-R, Chiang C-L, Ching-Tzong Su, Hwung H-R (2004) An induction motor position controller optimally designed with fuzzy phase-plane control and genetic algorithms. Electric Power Syst Res 68(2):103–112. https://doi.org/10.1016/S0378-7796(03)00159-7

Mohomad HH, Saleh SA, Chang L (2017) Disturbance estimator-based predictive current controller for single-phase interconnected PV systems. IEEE Trans Indu Appl 53(5):4201–4209. https://doi.org/10.1109/TIA.2017.2716363

Mosaad MI (2019) Optimal PI controller of DVR to enhance the performance of hybrid power system feeding a remote area in Egypt. Sustain Cities Soc 47:101469. https://doi.org/10.1016/j.scs.2019.101469

Mosaad MI (2019b) Maximum power point tracking of PV system based cuckoo search algorithm; review and comparison. Energy Proced 162:117–126. https://doi.org/10.1016/j.egypro.2019.04.013

Mosaad MI, Salem F (2014) Adaptive voltage regulation of self excited induction generator using FACTS controllers. Int J Ind Electron Drives 1(4):219–226. https://doi.org/10.1504/IJIED.2014.066211

Mosaad MI, Abu-Siada A, El-Naggar MF (2019) Application of superconductors to improve the performance of DFIG-based WECS. IEEE Access 7:103760–103769. https://doi.org/10.1109/ACCESS.2019.2929261

Mosaad MI, El-Raouf MO, Al-Ahmar MA, Bendary FM (2019a) Optimal PI controller of DVR to enhance the performance of hybrid power system feeding a remote area in Egypt. Sustain Cities Soc 47:101469. https://doi.org/10.1016/j.scs.2019.101469

Mosaad MI, Alenany A, Abu-Siada A (2020) Enhancing the performance of wind energy conversion systems using unified power flow controller. IET Gener Transm Distrib 14(10):1922–1929. https://doi.org/10.1049/iet-gtd.2019.1112

Pinzon JD, Colome DG (2019) Power system contingency ranking based on short term voltage stability indices. Latin Am Appl Res 49(4):225. https://doi.org/10.52292/j.laar.2019.92

Praiselin WJ, Edward JB (2017) Improvement of power quality with integration of solar PV and battery storage system based micro grid operation. Innov Power Adv Comput Technol. https://doi.org/10.1109/IPACT.2017.8245082

Prakash N, Jacob J, Reshmi V (2014) Comparison of DVR performance with Sinusoidal and Space Vector PWM techniques. Annual International Conference on Emerging Research Areas: Magnetics, Machines and Drives (AICERA/iCMMD). https://doi.org/10.1109/AICERA.2014.6908196

Rehman HU, Yan X, Abdelbaky MA, Jan MU, Iqbal S (2021) An advanced virtual synchronous generator control technique for frequency regulation of grid-connected PV system. Int J Electr Power Energy Syst 125:106440. https://doi.org/10.1016/j.ijepes.2020.106440

Shrivastav AK, Sadhu PK, Ganguly A (2019) Stability and harmonic analysis of a transient current limiter in distribution system. Microsyst Technol. https://doi.org/10.1007/s00542-018-3833-2

Wang Y, Yang Y, Fang G, Zhang B, Wen H, Tang H, Fu L, Chen X (2018) An Advanced maximum power point tracking method for photovoltaic systems by using variable universe fuzzy logic control considering temperature variability. Electronics 7(12):355. https://doi.org/10.3390/electronics7120355

Xiaofeng Xu, Wei Z, Ji Q, Wang C, Gao G (2019) Global renewable energy development: influencing factors, trend predictions and countermeasures. Resour Policy 63:1–15. https://doi.org/10.1016/j.resourpol.2019.101470

Zhao Q, Yin Z (2010) Battery energy storage research of photovoltaic power generation system in micro-grid," 2010 5th International Conference on Critical Infrastructure (CRIS), Beijing, China, 2010, pp. 1–4, doi: https://doi.org/10.1109/CRIS.2010.5617540

Zheng Z-X, Xiao X-Y, Chen X-Y, Huang C-J, Zhao L-H, Li C-S (2018) "Performance evaluation of a MW-Class SMES-BES DVR system for mitigation of voltage quality disturbances. IEEE Trans Ind Appl 54(4):3090–3099. https://doi.org/10.1109/TIA.2018.2823259